Bachelor Thesis



Czech Technical University in Prague

F3

Faculty of Electrical Engineering
Department of Control Engineering

Experimental system for magnetic levitation

with position and orientation control

Petr Šícho

Supervisor: Ing. Jiří Zemánek, Ph.D.
Field of study: Cybernetics and Robotics
May 2025

BACHELOR‘S THESIS ASSIGNMENT

I. Personal and study details

Student's name: **Šícho Petr** Personal ID number: **516399**

Faculty / Institute: **Faculty of Electrical Engineering**

Department / Institute: **Department of Control Engineering**

Study program: **Cybernetics and Robotics**

II. Bachelor’s thesis details

Bachelor’s thesis title in English:

Experimental system for magnetic levitation with position and orientation control

Bachelor’s thesis title in Czech:

Experimentální systém pro magnetickou levitaci s řízením polohy a rotace

Name and workplace of bachelor’s thesis supervisor:

Ing. Jiří Zemánek, Ph.D. Department of Control Engineering FEE

Name and workplace of second bachelor’s thesis supervisor or consultant:

Date of bachelor’s thesis assignment: **30.01.2025** Deadline for bachelor thesis submission: **23.05.2025**

Assignment valid until: **20.09.2026**

doc. Ing. Zdeněk Hurák, Ph.D.
Head of department’s signature

prof. Mgr. Petr Páta, Ph.D.
Vice-dean´s signature on behalf of the Dean

III. Assignment receipt

The student acknowledges that the bachelor’s thesis is an individual work.
The student must produce his thesis without the assistance of others, with the exception of provided consultations.
Within the bachelor’s thesis, the author must state the names of consultants and include a list of references.

Date of assignment receipt

Student’s signature

© ČVUT v Praze, Design: ČVUT v Praze, VIC

BACHELOR‘S THESIS ASSIGNMENT

I. Personal and study details

Student's name: **Šícho Petr** Personal ID number: **516399**

Faculty / Institute: **Faculty of Electrical Engineering**

Department / Institute: **Department of Control Engineering**

Study program: **Cybernetics and Robotics**

II. Bachelor’s thesis details

Bachelor’s thesis title in English:

Experimental system for magnetic levitation with position and orientation control

Bachelor’s thesis title in Czech:

Experimentální systém pro magnetickou levitaci s řízením polohy a rotace

Guidelines:

The aim of this thesis is to develop a physical model of a magnetic levitation system capable of stabilizing an object while controlling its elevation and orientation. The system will serve as a demonstrative tool for teaching automatic control principles.
Tasks:
1. Design and construct a magnetic levitation system that enables control over both the elevation and orientation of a levitating object.
2. Develop a mathematical model of the system, incorporating the magnetic field characteristics and the dynamic behavior of the levitating object.
3. Design and implement a control algorithm that ensures stable levitation and position and orientation control.
4. Build a demonstrative setup in which a levitating ball is used to create visual patterns in a medium such as sand.
5. Validate the system's performance through simulations and experimental testing.

Bibliography / sources:

[1] Berkelman, P., & Dzadovsky, M. (2011). Magnetic levitation over large translation and rotation ranges in all directions. IEEE/ASME Transactions on Mechatronics, 18(1), 44-52
[2] Subramaniam, A. B., Yang, D., Yu, H. D., Nemiroski, A., Tricard, S., Ellerbee, A. K., ... & Whitesides, G. M. (2014). Noncontact orientation of objects in three-dimensional space using magnetic levitation. Proceedings of the National Academy of Sciences, 111(36), 12980-12985.

© ČVUT v Praze, Design: ČVUT v Praze, VIC

FAKULTA ELEKTROTECHNICKÁ
FACULTY OF ELECTRICAL ENGINEERING
Technická 2
166 27 Praha 6

DECLARATION

I, the undersigned

Student's surname, given name(s): Šícho Petr
Personal number: 516399
Programme name: Cybernetics and Robotics

declare that I have elaborated the bachelor's thesis entitled

Experimental system for magnetic levitation with position and orientation control

independently, and have cited all information sources used in accordance with the Methodological Instruction on the Observance of Ethical Principles in the Preparation of University Theses and with the Framework Rules for the Use of Artificial Intelligence at CTU for Academic and Pedagogical Purposes in Bachelor's and Continuing Master's Programmes.

I declare that I used artificial intelligence tools during the preparation and writing of this thesis. I verified the generated content. I hereby confirm that I am aware of the fact that I am fully responsible for the contents of the thesis.

In Prague on 19.05.2025

Petr Šícho
.....
student's signature

Acknowledgements

I would like to thank my supervisor, Ing. Jiří Zemánek, Ph.D., for his valuable advice and consultations, which greatly helped me in the development of this thesis.

Abstract

This bachelor thesis presents the development of an experimental platform for magnetic levitation with integrated position and orientation control. The system combines permanent neodymium magnets and electromagnetic coils arranged in a modular configuration to achieve stable levitation of a magnet. Hall effect sensors are used for precise position measurements, and a STM32 microcontroller executes real-time PD feedback control to stabilize the levitating body in all three axes. Sensor signal compensation methods were implemented to counteract coil interference, ensuring reliable measurements. A finite element method (FEM) simulation was used to model the magnetic field and forces, aiding the design of a simplified analytical model for real-time control. The platform allows for adjustable height and rotational manipulation of the levitated object and is designed for future research and educational applications. The system demonstrates the feasibility of low-cost, open-source levitation technology with multiple degrees of freedom.

Keywords: magnetic levitation, position control, elevation and rotation, hall effect sensors, neodymium magnets, electromagnetic coils, PID control, finite element method (FEM), microcontroller (STM32), magnetic field modeling, sensor compensation, coil current regulation, real-time control, force modeling, analog-to-digital converter (ADC), modular platform design, magnetic dipole, H-bridge driver, system identification

Supervisor: Ing. Jiří Zemánek, Ph.D.

Abstrakt

Tato bakalářská práce se zabývá vývojem experimentální platformy pro magnetickou levitaci s integrovaným řízením polohy a orientace. Systém využívá kombinaci permanentních neodymových magnetů a elektromagnetických cívek uspořádaných v modulární konfiguraci k dosažení stabilní levitace magnetu. Pro přesné měření polohy jsou použity Hallovy sondy, zatímco mikrokontrolér STM32 zajišťuje zpětnovazební řízení v reálném čase pomocí PD regulátoru ve všech třech osách. Pro potlačení rušení od cívek bylo implementováno několik kompenzačních metod, umožňující rychlá a přesná měření. Magnetické pole a síly působící v systému byly odsimulovány pomocí metody konečných prvků, na základě čehož byl odvozen zjednodušený analytický model pro řízení v reálném čase. Platforma umožňuje nastavení výšky a rotace levitujícího tělesa a je navržena s ohledem na další budoucí výzkumné a vzdělávací využití. Výsledný systém potvrzuje proveditelnost dostupné a open-source magnetické levitace s více stupni volnosti.

Klíčová slova: magnetická levitace, řízení polohy, výška a rotace, Hallovy sondy, neodymové magnety, elektromagnetické cívky, PID regulace, metoda konečných prvků (FEM), mikrokontrolér (STM32), modelování magnetického pole, kompenzace senzorů, regulace proudu cívkami, řízení v reálném čase, modelování síly, analogově-digitální převodník (ADC), modulární návrh platformy, magnetický dipól, H-můstkový budič, identifikace systému

Překlad názvu: Experimentální systém pro magnetickou levitaci s řízením polohy a rotace

Contents

1 Introduction **1**
1.1 Motivation 1
1.1.1 Magnetic levitation 1
1.1.2 Related works 2
1.1.3 Aim of this project 2

2 Platform **5**
2.1 Working principle 5
2.2 Elements 7
2.2.1 Base plate 7
2.2.2 Hall sensor 7
2.2.3 Coils 8
2.2.4 Coil driver 9
2.2.5 Permanent magnets 10
2.2.6 Microcontroller 10
2.3 Sensors 11
2.3.1 Sensor differential module . . . 13
2.4 Coils 14
2.4.1 H-bridge driver 14
2.4.2 Coil current 15
2.4.3 Heat 16
2.4.4 Magnetic field 16
2.4.5 Force 18
2.4.6 Conclusions 19
2.5 Effect of coils on sensors 19
2.5.1 Static effects 19
2.5.2 Transient effects 20
2.5.3 Compensation 20
2.6 Microcontroller 23
2.6.1 Flow of the program 24
2.6.2 Key files and functions 24
2.6.3 Available serial commands . . . 25
2.6.4 Timers and PWM 26
2.7 Analog-to-digital converter 26
2.7.1 Analog read 26
2.7.2 External ADC 27
2.7.3 HAL ADC 27
2.8 Control 28
2.8.1 Experimentally tuning a PID regulator 28
2.8.2 Stable levitation 29
2.8.3 Automatic midpoint finder . . 29

3 Modeling **31**
3.1 Finite element method modeling 31
3.1.1 Force calculation 32
3.1.2 Meshing 33
3.1.3 Modeling the magnets 33
3.1.4 Modeling the coils 34
3.2 Results 35
3.2.1 Sensors readings 35
3.2.2 Transfer function of the platform 36
3.2.3 Force field of coils 38

4 Elevation and rotation **41**
4.1 Modular set 41
4.1.1 Parts 41
4.2 Elevation control 43
4.2.1 Principles 44
4.2.2 Individual coil control 44
4.2.3 Simple height control 44
4.2.4 Height measurements 44
4.2.5 Sensor readings in relation to height 46
4.2.6 Forces with relation to height 48
4.2.7 Height regulation 49
4.2.8 Lifting force of coils 49
4.3 Platform arrangements 50
4.3.1 6-coils arrangements 50
4.3.2 Lateral forces 51
4.3.3 Lifting forces 52
4.4 Rotation 53
4.4.1 Stabilizing rotation 53
4.4.2 Rotating pattern 54
4.4.3 Controlling rotation 54

5 Conclusion **55**
5.1 Applications 55
5.2 Achievements 56

A Images **57**

B Bibliography **63**

Figures

2.1 A boat placed on top of a magnet in white 3D-printed case, levitated above our platform. . . . 5
2.2 Up: The levitating magnet in a equilibrium. Bottom: The magnet disturbed from the equilibrium to the left. The coils respectively repulse and attract the magnet back to stable position. 6
2.3 Process diagram of the high-level working of the system. 6
2.4 Left: 3D printed base for the magnetic levitation prototype, Right: aluminum base plate. . . . 7
2.5 Diagram of the Hall effect sensor. Source [1]. 8
2.6 Coil with its dimensions. Source [2]. 9
2.7 Left: Neodymium magnet used for the base, Right: Neodymium magnet levitating above the platform. Source [3]. 10
2.8 Module (green) with two antiparallel Hall effect sensors for each of the two planar axis (black). 11
2.9 A magnet relative to one of the Hall sensors. 12
2.10 Circuit diagram used to process signals from Hall sensors. 13
2.11 Two of the circuits from 2.10 implemented on a circuit board with *LM324* quad-OPAMP [4]. . 14
2.12 Model of a real inductor as LR circuit. Source [5]. 15
2.13 Measuring magnetic induction above the device at height 22 mm above the center using the *QMC5883L* 3-axis Magnetometer. 17
2.14 Magnetic induction above the platform in the axis of the coil at distance 25 mm and height 24 mm, fitted with a linear function. Top: without any core (air core), Bottom: with a ferromagnetic core. 18
2.15 The effect of x-axis (top) and y-axis (bottom) coils on sensors. 21
2.16 Transient response of a coil pair to corresponding axis (blue) and perpendicular axis (brown) sensors. 22
2.17 Comparison of measured coil transient response and IIR filter to estimate the effect, at various sampling rates. 23

3.1 Meshing of the platform in COMSOL FEM, with infinite domain in yellow. The pyramid in the center acts as point positions of the Hall effect sensors. 32
3.2 Modeled lifting force of the passive magnet for various heights of the magnet. At $F = 0.63$ N, the magnet weight should be supported. 34
3.3 Simulated sensor readings for various positions measured from the center. 35
3.4 Measured force in the XY planes for various distances of the magnet from the center, with linear fit. 36
3.5 Measured force in the z-axis for various distances of the magnet from the center, with quadratic fit. 37
3.6 Measured force of a coil at $y = -20$ mm from the center carrying 1 A of current, for various positions of the magnet, fitted with the derived theoretical force function. 39

4.1 Modular set used to build the default 4-coil platform design alongside with a drawing with dimensions. 42
4.2 Magnet piece from the modular set with its Fusion model on the right. 42
4.3 Coil piece from the modular set with its Fusion model on the right. 43
4.4 Coil driver module with connector for coils (White), socket for the *DRV8874* POLULU driver (Black), LED overheating indicator and pins for configuration and connection to a microcontroller, view from top and bottom. 43
4.5 Height control of the levitating object. 45
4.6 Magnetic induction in relationship with height of the levitating magnet, fitted with power and quadratic functions. 46
4.7 Comparison of height and positional sensor readings with varying height. Top: magnet at the midpoint, Bottom: magnet displaced to $y = 5$ mm from the midpoint. 47
4.8 Comparison of radial force form magnets and force of one coil running at $I = 1$ A at $y = -20$ mm with the magnet at $y = -5$mm. 48
4.9 Effect of D regulator damping on oscillations in height. Top: undamped system, Bottom: system damped with D regulator. 49
4.10 Force projected on the magnet in z-axis depending on its height, using four coils with each running 1 A of current. 50
4.11 A drawing with dimensions of the base used to build a 6-coil platform. 51
4.12 Modular set used to build a 6-coil platform with coreless coils. 52
4.13 Lifting force of 4 coils running 1 A of current each based on their distance from the center of the platform. 52
4.14 Two added magnets to the levitation magnet in order to enable rotation. 53
4.15 Magnetic intensity norm above the coils, with the pattern above applied in the clockwise orientation. 54

5.1 A ball magnet levitated above the platform. 55

A.1 Current response of coils to step voltage. Voltage applied to coil in blue, coil current in brown (with a ration of 1.1 V/A). 57
A.2 Relationship between duty cycle and current, in *Phase* drive mode. 58
A.3 Relationship between duty cycle and current, in *Phase/Enable* drive mode with PWM frequency of 64 kHz. 58
A.4 Magnetic induction above the platform for coils with no core, fitted with a linear function, for all three axes. 59
A.5 Magnetic induction above the platform for coils with no ferromagnetic cores, fitted with a linear function, for all three axes. 60
A.6 Simulation of magnetic induction above the platform for coils with no core. 61
A.7 Simulation of magnetic induction above the platform for coils with no ferromagnetic cores. 61
A.8 Prediction of the coil force as given by Equation 3.16. 61

Tables

2.1 Coil parameters 9

July 30, 2026

Chapter 1

Introduction

1.1 Motivation

1.1.1 Magnetic levitation

Magnetic levitation (maglev) is a physical phenomenon in which an object is suspended above a surface with no physical contact, using magnetic forces to counteract gravity. The key advantage of magnetic levitation is the elimination of mechanical friction, which enables applications with very low wear, high speed, and high precision [6].

Principles

Several techniques are used to achieve magnetic levitation. Electromagnetic suspension relies on controlled electromagnets and feedback systems to adjust magnetic forces and maintain a levitated state. Electrodynamic suspension (EDS), on the other hand, generates lift through repulsive forces induced by the relative motion between moving magnets and conductors. Superconducting levitation exploits the Meissner effect, which expels magnetic fields from superconductors, enabling stable and strong levitation. Diamagnetic levitation uses materials that generate weak opposing magnetic fields but is generally limited to small-scale or demonstration purposes due to the very weak forces involved.

Magnetic levitation has found applications across many fields. In transportation, maglev trains use levitation to eliminate friction between the train and the track, allowing for smooth and high-speed travel. In industrial settings, magnetic bearings allow for the contactless support of rotating machinery, and magnetic levitation can be used for contactless melting of metals, preventing contamination from crucibles. Beyond the heavy industry, magnetic levitation is popular in consumer product displays to create floating and visually interesting object presentations. In advanced research and biomedicine, magnetic manipulation allows non-contact handling of delicate materials and biological samples with high precision [6].

Earnshaw's theorem

According to Earnshaw's theorem, stable static levitation of a body using only stationary paramagnetic materials (such as neodymium magnets or ferromagnetic materials) is impossible. This is because any arrangement of fixed magnetic fields will always result in an unstable equilibrium. This can sometimes be bypassed in systems involving motion or mechanical means of stabilization, for example, in maglev trains or the Levitron toy [7].

1.1.2 Related works

Magnetic levitation is already a well-described topic, even magnetic levitation with many degrees of freedom was achieved [8]. In most levitation systems, some way to support the weight of the levitation body has to be found. Some systems use suspension in a fluid [9], others use permanent magnets, and some opt for only using electromagnetic coils to suspend a magnet [8]. Another problem that needs to be solved in any magnetic levitation system is the measurement of the position. Most works on magnetic levitation focus on controlling the levitated object, while relying on expensive external measurement devices, including optical motion trackers [8], cameras [9]. Some levitation systems are upside down, with the levitation platform above the levitating magnet, use Hall effect sensors [10] or infrared receiver-emitters to measure the vertical distance. However, in this type of system, the platform only has to actively stabilize the levitating object in the vertical axis.

Magnetic levitation platform, stabilizing a magnet above a set of coils and permanent magnets, with no direct elevation or rotation control, can be bought online in a ready-to-use module [11]. We could not find any articles that describe this type of levitation platform, where the inner workings would be described. As the device is closed source, it is likewise impossible to modify, and usually only works with the specific levitating magnet to which it is fine tuned.

1.1.3 Aim of this project

This projects aims to create a electromagnetic suspension device, using a combination of permanent magnets and electromagnets in the base, able to levitate one permanent magnet above the base. The device should be minimalist and standalone, with only sensors incorporated in the base used and no external sensors placed around the device. In addition to this, we should be able to control the height of the levitation object and rotate it. In order to achieve rotation and height control, various arrangements and varieties of magnets and coils will be investigated.

This device will serve as a demonstational system, showing magnetic levitation with both height and rotational control in an open way, paving the way for future experimental research and educational use in automatic control. Our goal is to develop a highly reconfigurable and open platform that facilitates the creation of future magnetic levitation applications.

Outline

In the first part of the project, we build a prototype device capable of levitating the magnet in the center, without any control over rotation or height. Then we designed a modular set of building blocks for the levitation that can be used to quickly test different configurations of the platform - changing the number and positions of coils and permanent magnets, without the need to solder and manufacture the whole base of the platform every time. Using a finite element method (FEM) simulation software, we modeled the levitation platform numerically and used it to construct a simpler analytical model that could be used for real-time control. With these models, we were able to come up with a controller that resulted in a more stable levitation, with control over the elevation and rotation of the levitating object.

Chapter 2

Platform

An initial prototype demonstrating magnetic levitation above a stationary center was built and tested. It served as a proof of concept for further device development, such as elevation and rotation control.



Figure 2.1: A boat placed on top of a magnet in white 3D-printed case, levitated above our platform.

2.1 Working principle

Using permanent neodymium magnets placed in a circle around the base, we created a magnetic levitation platform that can lift another permanent magnet oriented with its magnetization in the same direction. However, this is an unstable position; the more the magnet moves to the center, the more it is attracted to one of the magnets, moving further away from the center and eventually collapsing into the magnet. Before this happens, we have to move the magnet back to the center position, which can be done using electromagnetic coils. This is illustrated in Figure 2.2 in one dimension. As the magnet moves off the equilibrium to the left, the right coil starts to attract the magnet, while the left coil repels it.

Hall effect sensors, placed in the center, are used to accurately measure the position of the magnet. As the coils also create a magnetic field that influences

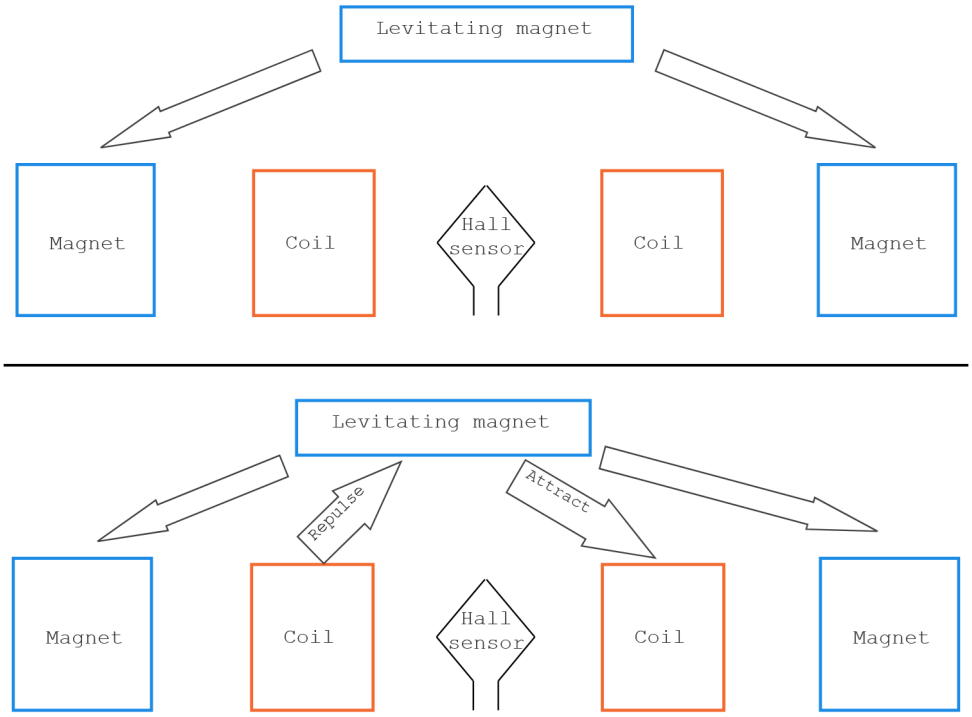


Figure 2.2: Up: The levitating magnet in a equilibrium.
Bottom: The magnet disturbed from the equilibrium to the left. The coils respectively repulse and attract the magnet back to stable position.

the reading from the Hall sensors, we will have to estimate this disturbance and compensate for it, in order to get reliable and accurate readings. The functioning of the system is depicted in a form of process diagram in Figure 2.3

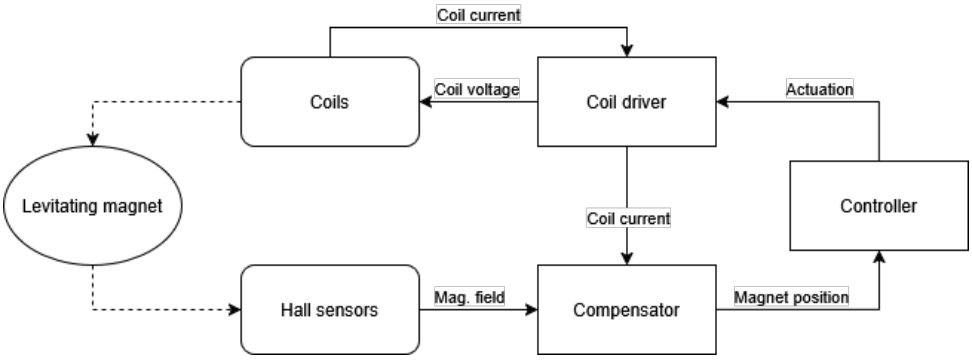


Figure 2.3: Process diagram of the high-level working of the system.

2.2 Elements

2.2.1 Base plate

A 3D printed base was used to fix the coils in a circle around the Hall effect sensors, enclosed in the small brown cylinder in the middle (in the newer version, this has a different appearance; see Figure 2.8), and then the neodymium magnets in an outer circle. This design was inspired by commercially available magnetic levitation platforms like those described in [11].

Since the coils generated significant heat during operation, which caused the plastic to soften and deform, we also experimented with an aluminum base to improve heat transfer and dissipation. Aluminum has a magnetic permeability very close to that of air or plastic, which made it seem like a good replacement for the 3D printed base. However, because aluminum is electrically conductive, eddy currents are generated inside the material, which affected the overall magnetic field disturbance caused by the coils in a way that was much harder to model and then compensate for. In the end, the use of a plastic or other non-conductive base proved to be necessary. Both of these variants are shown in Figure 2.4. In the future, using a printed circuit board with vias under the coils could be a good compromise, allowing for more efficient cooling.

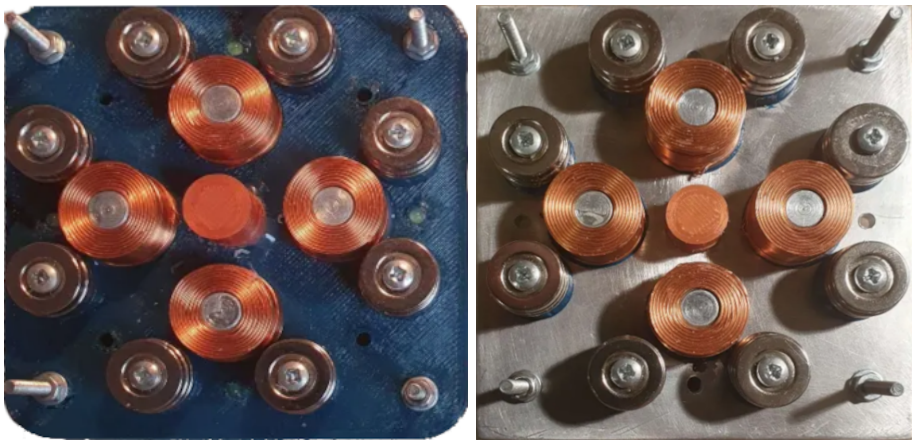


Figure 2.4: Left: 3D printed base for the magnetic levitation prototype, Right: aluminum base plate.

2.2.2 Hall sensor

The role of the Hall effect sensors will be to continuously measure the magnetic field associated with the levitating magnet positioned above the center of the platform. Accurate and low-latency positional measurements are critical for real-time feedback control, which would be hard to obtain using other type of sensors like ultrasonic rangers or cameras.

We choose the *SS49E* linear Hall effect sensor, that measures the magnetic induction B along the axis perpendicular to the flat side of the sensor, as shown in Figure 2.5 within a range of ± 1000 Gauss [1]. Given the strong magnetic fields produced by the levitating system, including the permanent magnets, the levitating magnet, and the electromagnetic coils, it was necessary to select a sensor with a sufficiently high range to prevent saturation.

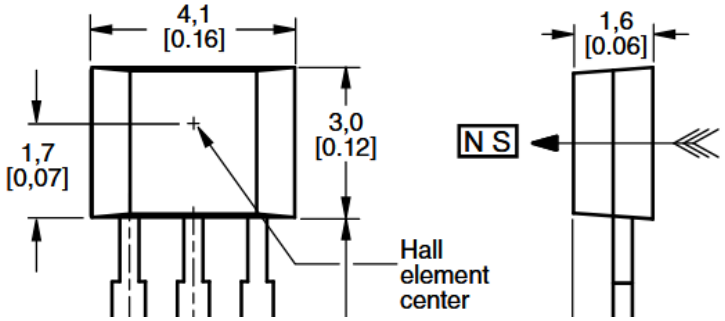


Figure 2.5: Diagram of the Hall effect sensor. Source [1].

In order to obtain the position of the magnet from the magnetic induction measurements, we have to account for the presence of substantial static and dynamic magnetic disturbances. The static component arises mainly from the permanent magnets placed around the base, while the dynamic component results from the rapidly varying fields generated by the coils. To subtract these effects, it was necessary to design and implement an active compensation mechanism. This compensator must effectively subtract the static bias introduced by the permanent magnets and, more importantly, dynamically correct for the time-varying magnetic fields produced by the coils.

2.2.3 Coils

Coils were used to generate a magnetic field that would either attract or repel the levitating magnet back to it's center position. We choose a type of coil that was already used in other magnetic levitation experiments [11] and that would be strong enough, with respect to the permanent magnets used, to sufficiently influence the levitating magnet. Each coil consists of about 500 turns of 28AWG coated copper wire (16 layers with 30 wounds of wire above), wound around a ferromagnetic core, as shown in Figure 2.6. Table 2.1 summarizes the important mechanical and electrical parameters of the coil.

The coil parameters were calculated using the current response to a voltage step of $V_{coil} = 12$ V that is displayed in the Appendix A.1. The resistance of the coil to the DC voltage is the voltage divided by the steady-state current $I_\infty = 2.34$ A, $R = \frac{U}{I_\infty} = 5.1\ \Omega$.

Inductance was determined from the equation for the time constant of an LR circuit $\tau = \frac{L}{R}$, which we measured to be 0.9 ms, corresponding to the time when the current reaches 63% of the steady state value [12]. This gives us $L = \tau R = 4.6$ mH. All measurements were performed with the coil kept

Table 2.1: Coil parameters

Parameter	Value
Inductance	4.6 mH
Resistance	5.1 Ω
Number of Turns	500
Height	12 mm
Diameter	19 mm
Core diameter	8 mm
Wire Diameter (AWG)	28 AWG

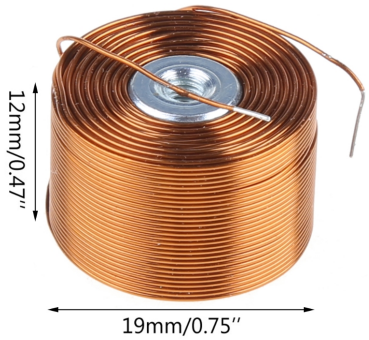


Figure 2.6: Coil with its dimensions. Source [2].

close to room temperature, as the resistance will increase when the coils heat up with continued use.

2.2.4 Coil driver

In order to accurately model and estimate the effect of the coils on the sensors and use them to exert a known force on the levitating magnet, we need to know the current running through the coils. Current sensors based on the Hall effect are not practical, as the external magnetic fields would affect the measurement. Either a driver with built-in current monitoring or an external shunt resistor seems to be the best variants for this case.

We choose the *DRV8874* H-Bridge Motor Driver with Integrated Current Sense and Regulation [13], in the form of a POLULU driver carrier [14]. This driver has an internal current mirror, allowing us to indirectly measure the current through the MOSFETs inside the H-bridge, outputting the current scaled by 450 µA/A, which can be measured with a precision resistor. For the POLULU driver carrier, they choose 2.49 Ω resistor to get a voltage of 1.1 V/A on the current sense pin [14], which can then be read by an analog-to-digital converter.

2.2.5 Permanent magnets

Two types of neodymium magnets were used in the experimental setup, both shown in Figure 2.7.

The first type consists of small ring-shaped magnets, stacked horizontally in groups of three and arranged in a circular pattern around the platform. Each magnet has an outer diameter of 14 mm, an inner diameter of 4 mm, and a height of 3 mm. The material used is NdFeB (Neodymium-Iron-Boron) with a grade of N38. The magnets are coated with a protective nickel layer to prevent corrosion.

The second type is a single disc-shaped magnet that is intended to be levitated above the platform. This magnet has a diameter of 35 mm and a height of 5 mm. It is also fabricated from NdFeB material, with a higher grade of N42. The surface is likewise protected by a nickel coating. The mass of the disc magnet is 36 g. To protect the magnet from mechanical impacts, it was placed inside a custom-designed 3D printed enclosure, as neodymium magnets are relatively brittle and susceptible to damage during operation.

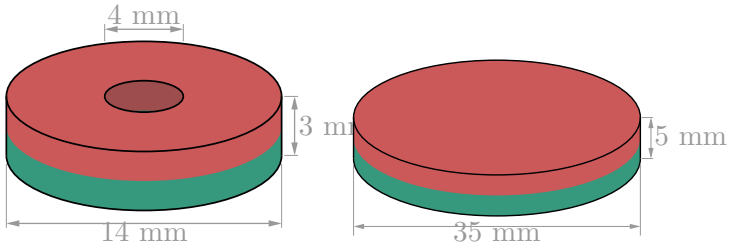


Figure 2.7: Left: Neodymium magnet used for the base, Right: Neodymium magnet levitating above the platform. Source [3].

With the protection enclosure and 3D toy ship, the whole levitating body weights 63 g.

2.2.6 Microcontroller

An *STM32F411RE* microcontroller on a NUCLEO-64 board was used, providing sufficient computational power to run the control algorithms and enough pins to control the coil drivers actuating the coils and read sensors. The microcontroller features an ARM Cortex-M4 core with 512 KB of Flash memory and 128 KB of SRAM, running at up to 100 MHz, which enables us to run even more sophisticated control algorithm quickly enough to react smoothly to change in position. It also includes a 12-bit ADC with 16 channels and a sampling rate of up to 2.4 MSPS, enabling quick and precise analog voltage measurements, used for reading the Hall effect sensors and current from coil drivers. For controlling the driver with pulse-width modulation (PWM), the *STM32F411RE* offers 11 timers, including six 16-bit timers and two 32-bit timers [15].

2.3 Sensors

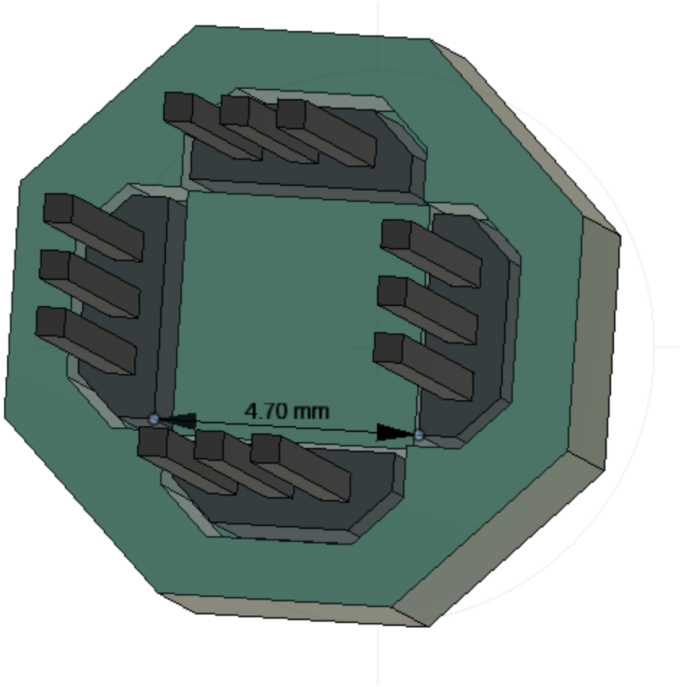


Figure 2.8: Module (green) with two antiparallel Hall effect sensors for each of the two planar axis (black).

In order to measure the position of the magnet around the center of levitation as precisely as possible, we used two Hall effect sensors in antiparallel orientation for each of the two planar axis. They are mounted in a 3D printed enclosure shown in Figure 2.8, which was attached to the base in such a way that it's height can be adjusted. With two sensors on each axis, we can effectively double the resolution of our readings and remove the static component of the magnetic field, as we will now demonstrate.

In general, the magnetic induction $\vec{B}$ generated by the magnetic dipole of the permanent magnet at point $\vec{r}$ from the center of the magnet will be

$$\vec{B} = \frac{\mu_0}{4\pi}\left(\frac{3\vec{r}(\vec{m}\cdot\vec{r})}{r^5} - \frac{\vec{m}}{r^3}\right), \tag{2.1}$$

where $\vec{m}$ is magnetic moment and μ_0 vacuum permeability [16, p. 146–150].

In our case, let us assume that the permanent magnet is placed with its vector of magnetization exactly perpendicular to the base, and placed at a height h above the center of the Hall effect module, so at a horizontal distance d from each Hall effect sensor.

Considering the magnetic induction only in the XY plane, where the measurements will be performed, this can be simplified neglecting the z-component as

$$\vec{B}_{xy} = \frac{3\mu_0}{4\pi}\frac{\vec{r}(\vec{m}\cdot\vec{r})}{r^5}\,. \tag{2.2}$$

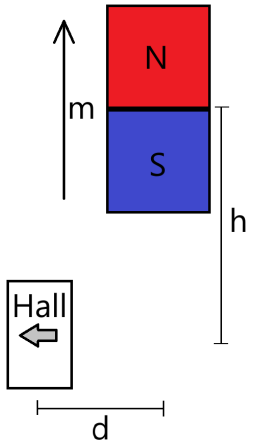


Figure 2.9: A magnet relative to one of the Hall sensors.

For calculating the magnetic induction measured by one of the sensors, let us choose, without loss of generality, the left x-axis sensor and denote the component of $\vec{B}$ measured by it as B_x. The relative position of the Hall effect sensor and the magnet is depicted in Figure 2.9. Since the magnetic moment $\vec{m} = \vec{m}_0 m$ is pointing straight up, the scalar multiplication $\vec{m}\cdot\vec{r}$ becomes hm. Furthermore, we will suppose that $h \gg d$, which holds as the magnet will levitate at tens of millimeters above the sensor, while the relative displacement of the magnet will be only a few millimeters. We can then rewrite $r^5 = (d_x^2 + h^2)^{5/2} = h^5(1 + d_x^2/h^2)^{5/2}$, where $d_x^2/h^2 \ll 1$, as $r^5 \approx h^5 + \frac{5}{2}d_x^2 h^3 \approx h^5$. The whole expression then becomes

$$B_x = \frac{3\mu_0}{4\pi}\frac{d_x m h}{h^5} = \frac{3\mu_0}{4\pi}\frac{1}{h^4}d_x\,, \tag{2.3}$$

which is linear in d_x.

For a magnet that has moved by Δd_x in the positive direction of x axis, the two antiparallel Hall sensors will respectively perceive magnetic inductions

$$B_{x1} = \frac{3\mu_0}{4\pi}\frac{1}{h^4}(d_x - \Delta d_x)\,,$$

$$B_{x2} = -\frac{3\mu_0}{4\pi}\frac{1}{h^4}(d_x + \Delta d_x)\,.$$

We will use this fact to double the resolution of reading $\frac{3\mu_0}{4\pi}\frac{1}{h^4}\Delta d_x$, while disregarding the much larger $\frac{3\mu_0}{4\pi}\frac{1}{h^4}d_x$.,

$$B_{sens\_x} = B_{x1} + B_{x2} = \frac{3\mu_0}{2\pi h^4}\Delta d_x\,. \tag{2.4}$$

The derivations and equations presented in this section assume that the magnet is small and far away, where we can use the dipole model. In order to verify to what extent these assumptions hold in our case, we will perform simulations and verify them experimentally in Section 3.2.1.

Throughout the rest of the thesis we will assume a coordinate system centered on the sensors in the middle of the platform, with the height $h = 0$ set to the top edge of the coils.

2.3.1 Sensor differential module

The sensors are in opposite orientation, so the magnetic induction read by them will have opposing signs. For this reason, in order to extract the change $\Delta B_x = \frac{3\mu_0}{4\pi}\frac{1}{h^4}\Delta d_x$, we need to subtract their readings.

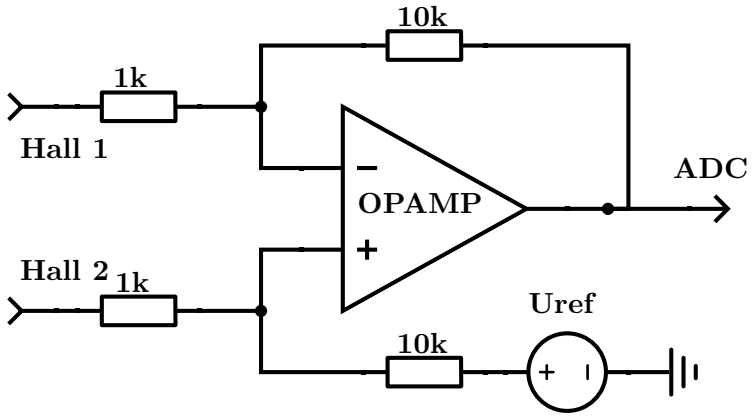


Figure 2.10: Circuit diagram used to process signals from Hall sensors.

To perform this calculation, a differential amplifier implemented with an operation amplifier (OP AMP) was used. To further amplify the reading and reduce the error of ADC conversion, the difference was multiplied by a factor of 10. As the OP AMP is powered by +5 V, we were unable to capture the negative part of the difference. That is why the resulting voltage is offset by U_{ref} [12]. The circuit used is depicted in Figure 2.10. In conclusion, considering the sensitivity of the Hall effect sensor $k_{hall} = 1.4$ mV/Gauss[1] the voltage read from this circuit is proportional to the relative displacement of the magnet with constant $k = 20 \cdot k_{hall} \cdot \frac{3\mu_0}{4\pi}\frac{1}{h^4}$,

$$U_x = U_{ref} + k \cdot \Delta d_x \,. \tag{2.5}$$

A practical implementation on a universal circuit board is visible in a picture in Figure 2.11, using the *LM324* quad operational amplifier [4].

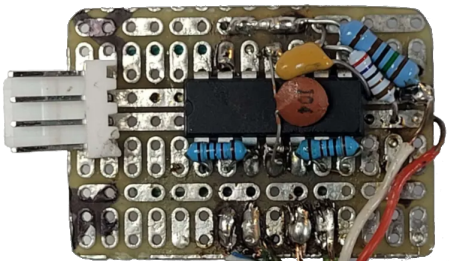


Figure 2.11: Two of the circuits from 2.10 implemented on a circuit board with *LM324* quad-OPAMP [4].

2.4 Coils

2.4.1 H-bridge driver

The *DRV8874* H-Bridge driver has three input pins that we can use to control it for our use case. There is a *Phase* pin, that is used to set the direction of the actuation and*Enable* pin that will turn the output on and off, and both can be controlled with a PWM signal from the microcontroller. Finally with *Vref* pin we can set the current limiting. This allows principally three ways of controlling the motor.

- Phase / enable mode - use a digital pin to set the direction on *Phase* pin, then with a PWM pin actuate *Enable* pin to control the voltage applied to coil. When the *Enable* pin is *LOW*, the driver enters brake mode with the coil terminals shorted and the current is dissipated naturally in the coil.
- Phase mode - with the *Enable* pin tied to *HIGH*, we control the driver with only *Phase* pin using PWM. When using a duty cycle of 50%, the driver will constantly change direction, resulting in almost no current flowing. With an increase or decrease in the duty cycle, the coil will spend more time in one of the phases, resulting in a gradually increasing current.
- Vref mode - the *Enable* pin is once again set *HIGH* and we control the direction of drive with *Phase* pin normally. By sending a PWM signal to *Vref* pin, we set the maximum current limit and let the driver handle the current limiting on it's own.

In both the Phase and Phase/Enable modes, the relation between PWM duty cycle and current was measured to be almost linear, assuming constant coil temperature, with some area of deadzone and saturation.

However, in Phase mode, when the phase is different from the direction of current in the coil, the current flows through the reverse diodes of the MOSFET drivers and is not registered by the internal current mirror [13]. This means that the *IPROPI* pin shows the true value only a fraction of the

time and reads zero otherwise. When measuring multiple times and averaging, the results are skewed accordingly, as is shown in Appendix A.2. Although this is not hard to compensate for, it increases the time and computations needed to read the current value.

On the other hand, while the Phase / Enable mode requires two pins to interface, the current can be read directly at all times [13], making it a better option. The measured duty cycle - current relationship is available in Appendix A.3, where the deadzone is visible.

The *Vref* mode seems to combine the best of both worlds, providing automatic current regulation, that works independently of the coil temperature. However, during testing, we were unable to make it work with a PWM signal applied to the *Vref* pin. The high-frequency PWM seemed to induce significant disturbance in the analog circuitry of the driver. Only after smoothing with an RC lowpass filter was this technique usable, but this also negatively impacted the reaction time of the driver.

Due to its simplicity and reliability, the Phase/Enable mode was used. The accurate and immediate current reading we could get in this mode was instrumental in making the coil effect compensation on the Hall sensors fast and precise enough.

2.4.2 Coil current

In a simple electrical model [5, chap. 6], we can split the coil into a perfect inductor with inductance L and a series resistor with resistance R as shown in Figure 2.12.

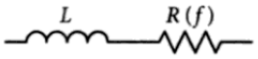


Figure 2.12: Model of a real inductor as LR circuit. Source [5].

The resistance $R(f)$ corresponds to the DC resistance of the wire only at low frequencies, where the skin and proximity effects do not come into play [5]. This should also hold in our case, as the control algorithm will run at only a few kilohertz speeds.

The current passing through the circuit can be described as

$$i(t) = \frac{U}{R}\left(1 - e^{-Rt/L}\right) = \frac{U}{R}\left(1 - e^{-t/\tau}\right), \tag{2.6}$$

where the time constant τ is defined as $\tau = \frac{L}{R}$ [12].

This circuit can be further rewritten using the Laplace transform [12] as a first-order system with one pole at $s = -R/L$, which acts as a low-pass filter on voltage:

$$I(s) = \frac{1}{R + Ls}U(s) = \frac{U(s)}{R}\frac{1}{1 + sL/R} = \frac{U(s)}{R}\frac{1}{1 + \tau s}. \tag{2.7}$$

PWM frequency

When driving the coil by PWM, we will profit from the inherent low-pass filtering of the coils, as the current at the coil will be smoothed out, with a high enough PWM frequency. As we want the reading and magnetic field produced by the coil to be as smooth as possible, the higher the PWM frequency, the better. We will choose 64 kHz, in order not to exceed the frequency limits of the H-bridge driver [13]. With the time constant of the coil being 0.9 ms, this gives us attenuation of −25 dB.

Current sign

As the current output of the driver is without sign, we cannot directly tell in which direction is the current passing. We will try to infer this from the direction of supply voltage. In case of abrupt changes in the phase, the current will follow only after some time, dropping to zero and then rising again. The microcontroller samples the current value only roughly once every 200 µs, depending on the specific control and compensation algorithm. We have to choose an area around zero, where we will flip the sign of the current according to the direction of the voltage, and otherwise remember it.

2.4.3 Heat

One of the problems with the prototype of magnetic levitation was the heating of the coils as the current was running through them. Using the LR model described in Figure 2.12 , the resistor will produce a Joule's heat when current I is passing through the circuit equivalent to

$$P = I^2 R\,. \tag{2.8}$$

This gives us a strong incentive to minimize the current passing through the coils, as the heat produced scales with a square of current. Throughout our experiments with the platform, we would closely monitor the coil currents and try to find a control algorithm that would minimize it. [12]

2.4.4 Magnetic field

Knowing how the magnetic field of the coils behaves will be crucial to compensating its effects on sensors and estimating the force exerted on the levitating magnet.

As was shown in [17] we can split the magnetic inductance generated by a coil into it's positional (r) component and current-depended (i) component as

$$B_{coil}(i, r) = f(i) B_{ref}(r)\,. \tag{2.9}$$

Current-dependent relationship

In order to determine the shape of the function $f(i)$ from Equation 2.9, we would measure the magnetic field using a *QMC5883L* 3-Axis Magnetometer placed at a height of 22 mm above the edge of the coils in the center of the platform, which should correspond to the location of the levitating magnet, as shown in Figure 2.13.

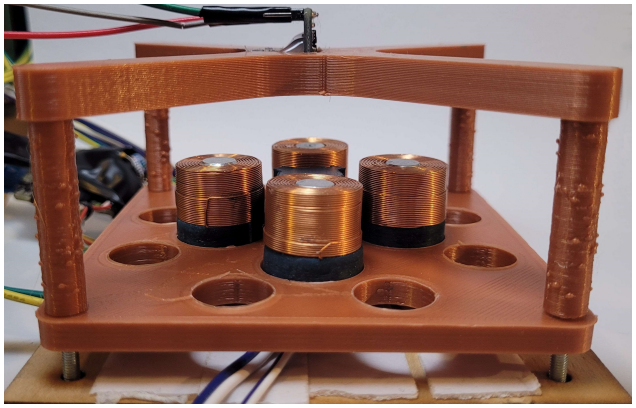


Figure 2.13: Measuring magnetic induction above the device at height 22 mm above the center using the *QMC5883L* 3-axis Magnetometer.

The measurements were performed both for coils with the ferromagnetic core and also with the core removed. Without the core, the measured relationship was linear with Root mean square error (RMSE) of 0.027 G. The core adds non-linearities to the current - magnetic induction relationship, for example due to magnetic saturation of core. The data were also fitted with a linear function, this time with RMSE of 0.253 G. Both of the measurements in one axis are displayed in Figure 2.14. All the measurements from all three axes of magnetic induction with their respective linear fits are available in the Appendix A.4 and A.5.

From the data gathered, which we will also verify using FEM simulation in the following chapters, we can estimate that $f(i)$ is a linear function of the current $f(i) = k_{curr}i$. Thus Equation 2.9 becomes

$$B_{coil}(i, r) = k_{curr}i \cdot B_{ref}(\vec{r})\,. \tag{2.10}$$

Position-dependent relationship

Similarly to [17], we will model the coil as an infinitesimally thin and infinitely long magnet, which corresponds to a magnetic monopole placed somewhere inside the coil. The magnetic induction that is generated by the magnetic charge will be

$$B_{ref}(r) = \frac{q_m}{4\pi}\frac{\vec{r}}{|r|^3}\,. \tag{2.11}$$

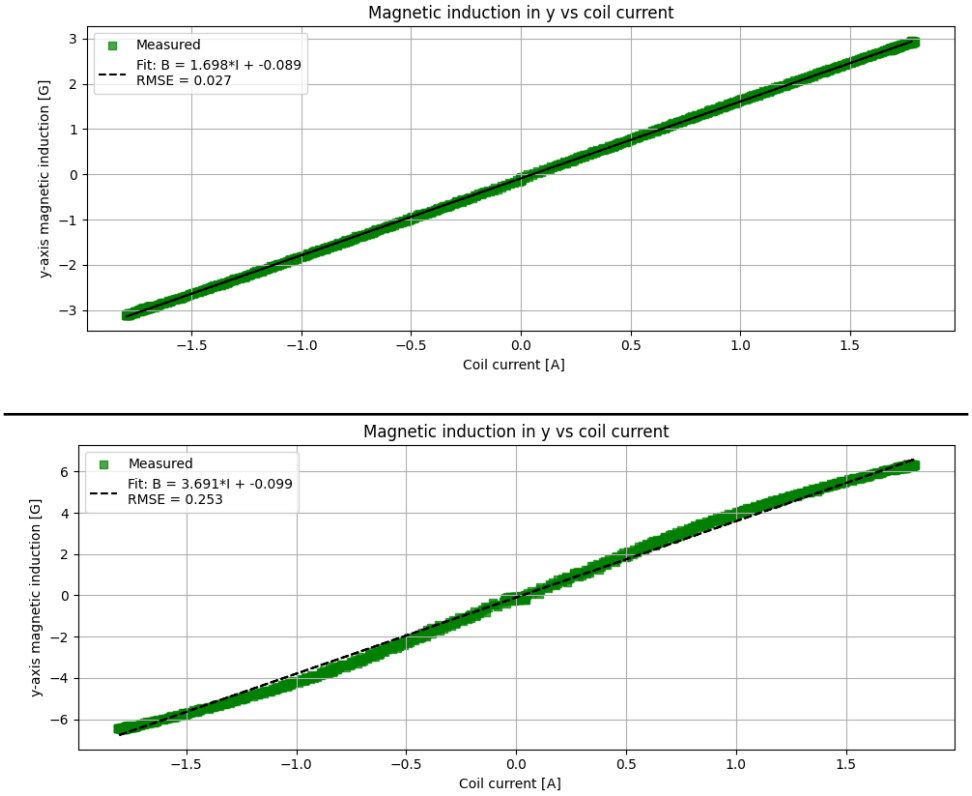


Figure 2.14: Magnetic induction above the platform in the axis of the coil at distance 25 mm and height 24 mm, fitted with a linear function.
Top: without any core (air core), Bottom: with a ferromagnetic core.

By plugging this model into Equation 2.10, we get the final expression for magnetic induction

$$B_{coil}(i,r) = i \cdot \underbrace{k_{curr}(\frac{q_m}{4\pi}}_{k_{coil}} \frac{\vec{r}}{|r|^3}) = ik_{coil}\frac{\vec{r}}{|r|^3}\,. \tag{2.12}$$

2.4.5 Force

We are interested in the force that our coils exert on the permanent magnet that levitates above the center of the platform. Generally, the force on a magnetic dipole in a non-uniform magnetic field is

$$F = (\vec{m}\cdot\nabla)\vec{B}\,, \tag{2.13}$$

where $\vec{m}$ stands for effective magnetic dipole of the permanent magnet [17]. Plugging in the results from Equation 2.10, we get a linear relationship between the force and current of a coil

$$F = ik_{curr}(\vec{m}\cdot\nabla)B_{ref}(\vec{r})\,. \tag{2.14}$$

Using the monopole model of the coil, the force acting on the magnet can be estimated as

$$\vec{F} = ik_{coil}\left[\frac{\vec{m}}{r^3} - 3 \cdot \frac{(\vec{m}\cdot\vec{r})\vec{r}}{r^5}\right] . \tag{2.15}$$

Considering that the magnets dipole points in the z direction we can write $\vec{m} = (0, 0, m)$ and further simplify the force calculation as

$$\vec{F} = ik_{coil}m\left[\frac{(0,0,1)}{r^3} - 3 \cdot \frac{z}{r^5}\vec{r}\right] . \tag{2.16}$$

Forces in the x and y directions will be

$$\vec{F}_{xy} = -3ik_{coil}m\left[\frac{z}{r^5}\vec{r}\right] . \tag{2.17}$$

We will obtain force measurements from a Finite Element Method (FEM) simulation, described in a later chapter, calculating the force from the Maxwell stress tensor [18]. The high computational demands of these simulations make them unusable for real-time control applications. However, the results from these simulations are useful in order to fit the much simpler analytical model derived in Equation 2.17.

2.4.6 Conclusions

An interesting conclusion we can already draw from Equation 2.14 is that the force exerted on the magnet scales linearly with the current, while the power consumption of the coil, and more importantly the heat produced by them (Equation 2.8), grows with a square of current. This hints us that using more coils could be beneficial in reducing the power consumption and cooling needs of the coils and would allow finer control over the magnet.

2.5 Effect of coils on sensors

The magnetic field created by the coils affected the readings from the Hall effect sensors. In order to get accurate reading from the sensors, we need to make them resistant to this interference.

2.5.1 Static effects

To measure this effect, we would run a specified current for a set amount of time and examine how much has the output from the Hall effect sensors changed in a each axis (0 to 1024 corresponding to 0 V to 5 V reading from the sensor module). The effect is visible for the x-axis coils and the y-axis coils in Figure 2.15. All points were measured twice, starting at actuation of +100%, going to -100% and then back to 100%, to account for magnetic hysteresis of the coil. This is visible as the area between the two lines, where the core remains magnetized and influences the sensor reading. At each

PWM actuation we would wait for 20 ms to eliminate the transient response of the coil. Some small area of deadzone is around the center of the graph, where a magnetic field is generated, but we do not measure any current. The saturation of the current sensor is also visible at the edges at 3 A, which corresponds to the maximum ADC voltage level of 3.3 V [15].

As the magnitude of this effect is on the same order as when the magnet is moved around, we will have to find a way to compensate for these effects to get usable readings.

2.5.2 Transient effects

We have also measured how the sensors react to fully charging the coil in Figure 2.16. The shape of this curve was found to match very closely with the current response curve of the curve, measured previously in Figure A.1. This result is in line with Equation 2.10, which describes the relationship between magnetic induction and current.

2.5.3 Compensation

We tried several approaches to compensating the coil effect, based on the results measured and derived in the previous subsection.

Voltage-based compensator

One way is to estimate the effect of coils based on the PWM duty cycle, assuming a time-independent linear relationship between the duty cycle and the current. Upon reaching a stable temperature, the current should follow the curve measured in Figure A.3, then the interference will match what was measured in Figure 2.15.

We tried a linear compensation method, assuming that sensor inference is proportional to duty cycle, which should hold for the region -1.5 A to 1.5 A, where the coils will operate for the majority of time, to avoid overheating. Then we tried to compute an exact mapping - measuring and remembering the sensor inference for each duty cycle.

This was the quickest method, as it did not require measuring the coil currents, as taking measurements with the ADC is the most time-consuming operation, which will be discussed in more detail in Section 2.7. However, it needed calibration with the operation-hot coils and its performance deteriorated when the temperature of the coils changed. Another problem was the lack of modeling of transient effects, which we tried to correct by implementing an IIR model of the transient response of the coils.

IIR compensator

The coil acts as a low-pass filter from voltage to current (and thus magnetic induction) as described in Equation 2.7. We will discretize this equation for

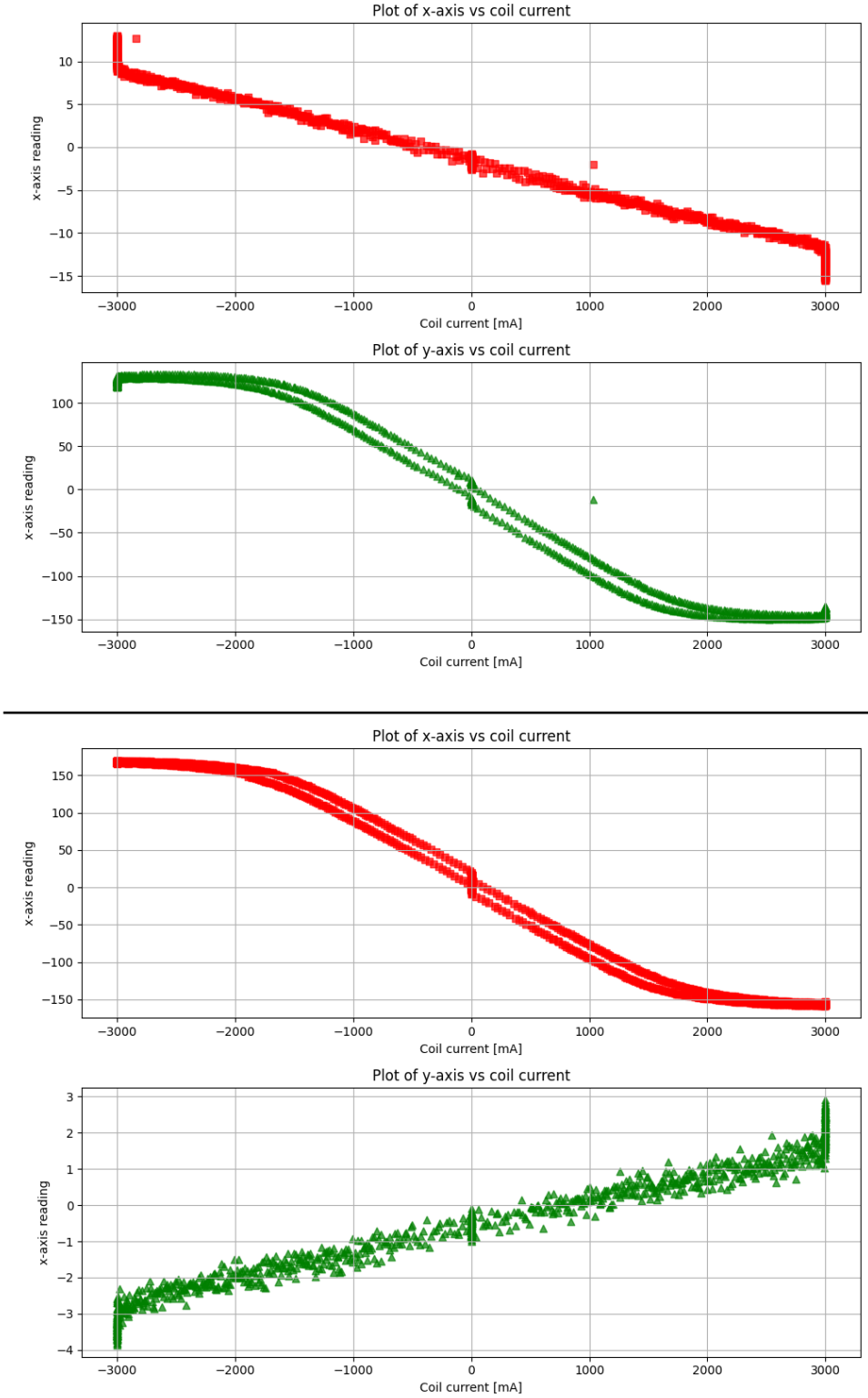


Figure 2.15: The effect of x-axis (top) and y-axis (bottom) coils on sensors.

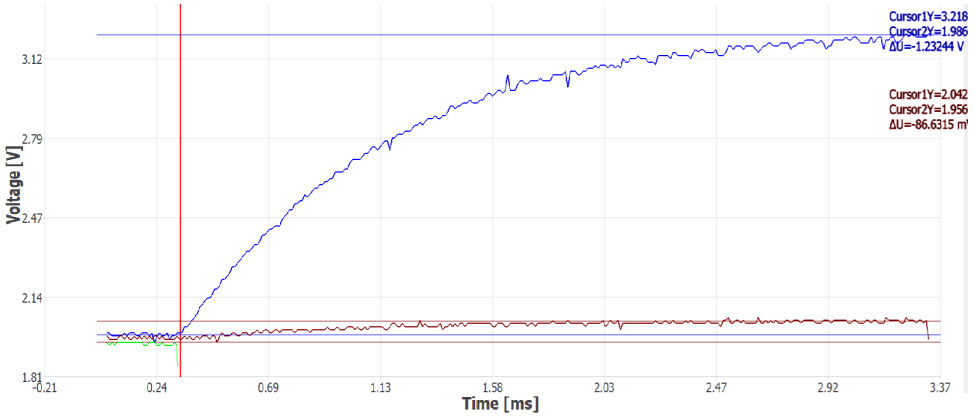


Figure 2.16: Transient response of a coil pair to corresponding axis (blue) and perpendicular axis (brown) sensors.

sample time T_s this using the backward Euler method, substituting $s = \frac{z-1}{T_s z}$, Equation 2.7 thus becomes

$$I(z) = \frac{U(z)}{R} \frac{T_s z}{(\tau + T_s)z - \tau} = \frac{U(z)}{R} \frac{T_s}{\tau + T_s - \tau z^{-1}} \,. \tag{2.18}$$

We will rewrite this further as an IIR filter than we can then implement with a microcontroller:

$$y[n] = \frac{\tau}{R(\tau + T_s)} y[n-1] + \frac{T_s}{\tau + T_s} x[n] \,. \tag{2.19}$$

To evaluate the performance of the filter, a 12 V voltage step is applied with a delay of one sampling interval - accounting for the measurement delay of the Hall effect sensors on the microcontroller - and the result is compared to the measured response shown in Figure 2.16. The performance of the filter depends on the sampling time, as is shown in the comparison below in Figure 2.17, with the best match being at 5 kHz. Nonetheless, the sampling time of our microcontroller depends mainly on the speed of the ADC converter and cannot be freely chosen.

Using a combination of the IIR compensator for transient effects and voltage-based compensator of static effects, we were able to compensate the effect of the coils to such an extent as to obtain clear readings, enabling control and levitation. However, both of these compensators rely on the constant resistance of coils, which will change with temperature. In the first prototypes of the device, the coils heated up greatly, rising from room temperature to 60 °C in about 2 minutes, where the compensator model usually differentiated from reality to such an extent that the device stopped working.

Current-based compensation

Another approach is to use the current measured from the coil drivers to calculate the compensation from the responses measured in Figure 2.15. This

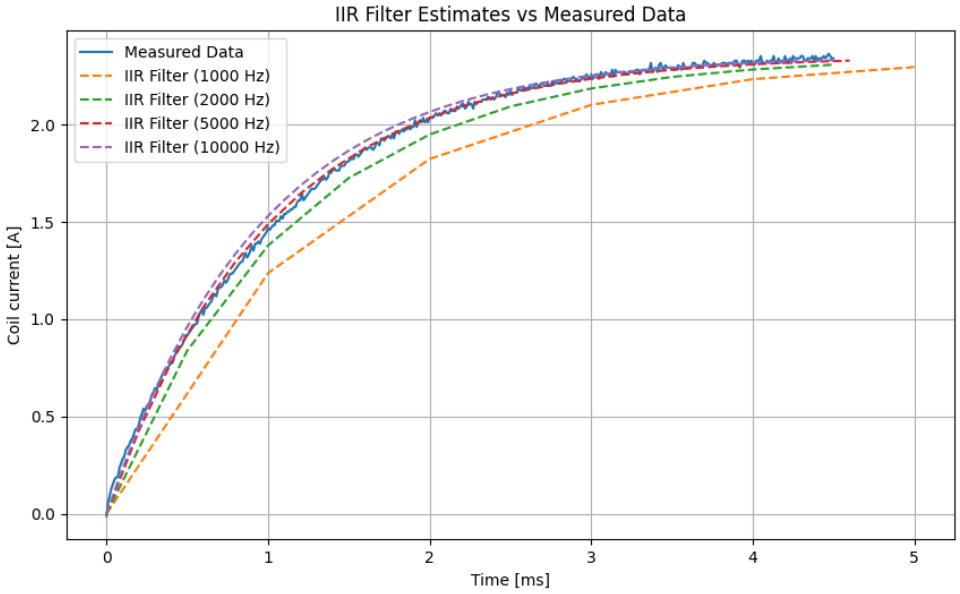


Figure 2.17: Comparison of measured coil transient response and IIR filter to estimate the effect, at various sampling rates.

would eliminate the problem of changing coil parameters and would also follow the transient coil response without the need for simulation with an IIR filter. This makes it a more general model, without many constants, that works seamlessly even for different coils and setups.

In the same way as with the voltage-based compensator, we implemented both linear and exact mapping compensator. They both worked well for eliminating steady-state difference, with most of the errors coming from the coil hysteresis. The compensator was nevertheless greatly affected by the speed of our system, mainly caused by making many ADC measurements. As the measurements take up a long time, the order in which they were taken influenced the error. We experimented with changing the sequence of measurements, reaching the conclusion that it is better to first measure the current and then the Hall sensor for each axis.

2.6 Microcontroller

To control the magnetic levitation system in real time, a program was developed and implemented on the *STM32F411* microcontroller. This code is responsible for processing sensor measurements, executing control algorithms, and generating appropriate actuation signals to stabilize the levitated object, according to the process diagram in Figure 2.3.

The code was written in *C++* using both the STM32 HAL (Hardware Abstraction Layer) library where necessary for quick hardware control and Arduino libraries for more concise and readable code.

2.6.1 Flow of the program

The program operates by initializing all necessary components in the `setup` function, which includes setting up hardware, sensors, PID controllers, and serial communication. The main logic resides in the `loop` function, which continuously executes to maintain the system's operation and levitation of the magnet. Position readings are obtained and fed into the PID controllers to compute adjustments for the magnetic field, applied by controlling the coil currents. The state of the system is logged and communicated via the serial interface, enabling real-time monitoring and debugging. Additionally, the program listens for serial commands that allow for dynamic configuration, calibration, and measurements, testing of newly implemented features, or activation of specific modes for making more advanced measurements with the system.

2.6.2 Key files and functions

- `Levitator.ino`:
  - Acts as the main entry point to the system.
  - Relies on subsystems like `serial`, `hardware`, `controller`, and `sensor` for functionality.
  - Implements `setup` and `loop` functions to initialize components and run the main program loop.
- `define.h`:
  - Defines the `State` structure for storing system state (e.g., coil currents, positions, timing, etc.).
  - Declares namespaces (`serial`, `sensor`, `hardware`, `controller`, `utils`) and their respective functions.
- `controller.ino`:
  - Contains PID controller logic.
  - **Functions**:
    - `setup`: Configures the PID controller parameters.
    - `pid`: Executes PID computations.
    - `regulate`: Adjusts coil actuation based on PID outputs.
- `hardware.ino`:
  - Manages direct interaction with hardware - coils and sensors.
  - **Functions**:
    - `setup`: Initializes the ADC, coil, and sensor pins.
    - `readADC`: Measures quickly analog values from a ADC channel.
    - `measure`: Measures precisely the analog value of a pin.

    - `write_coil`: Writes intensity values to a specific coil, ranging from −255 to 255.
    - `clear_coils`: Resets all coils.

- `sensors.ino`:
  - Handles sensor readings, compensation, and calibration.
  - **Functions**:
    - `setup`: Initializes the compensator.
    - `calibrate`: Calibrates sensors and compensators of coil effects.
    - `calibrate_midpoint`: Calibrates the position sensor midpoint.
    - `read_values`: Read the values from Hall sensors and current from coils, applies compensation, and calculates the magnet position.

- `serial.ino`:
  - Manages serial communication, debugging, and plotting values.
  - **Functions**:
    - `setup`: Initializes serial communication.
    - `serial_commander`: Handles incoming serial commands.
    - `print_current_state`: Prints the current state of the system.

- `utils.ino`:
  - Provides utility functions for debugging, analysis, and special modes.
  - **Functions**:
    - `average_analysis`: Calculates running averages for analyzing states and variables.
    - `debug_state`: Prints debug information about the state of the system.
    - `debug_current`: Prints the actual current usage of all the coils.
    - `special_mode`: Activates special modes for measuring, testing, or calibration.

2.6.3 Available serial commands

- `C[coil] [value]`: Sets directly the intensity of a specific coil, from 0 to 510, where 255 represents no current flow.
- `P`: Toggles the print mode for real-time debugging.
- `M`: Recalibrates the sensor midpoint.
- `B`: Increments the printout buffer. This saves system states to buffer without slowing it down by printing them immediately.
- `O`: Prints all the states saved in the printout buffer.

- `R`: Recalibrates the entire system, including coil compensation.
- `S[coil]`: Activates a special mode for testing or calibration on a specified coil.
- `L`: Starts or stops levitation and recalibrates the sensor midpoint before starting.
- `L0`: Toggles levitation ON/OFF without recalibrating midpoint
- `+[variable] [value]`: Increases the specified variable by the given value. Used for testing new features and debugging.
- `-[variable] [value]`: Decreases the specified variable by the given value. Used for testing new features and debugging.

2.6.4 Timers and PWM

The *STM32F411* microcontroller provides six independent timers (*TIM1*, *TIM2*, *TIM3*, *TIM4*, *TIM5*, and *TIM9*) capable of generating PWM signals with individually adjustable duty cycles and frequencies [15][19, file STM32F411R(C-E)T PeripheralPins.c]. However, in the Arduino environment, with the default `analogWrite()` function, we were unable to use more channels per timer while a custom frequency was specified. Consequently, to achieve independent PWM signal generation, it was necessary for each output pin to have a different timer. In particular, by default, only four timers are broken out to accessible pins on the *Nucleo-F411RE* development board. To make use of the six timers, it is necessary to manually configure alternative pin functions, such as enabling the `PB8_ALT0` and `PB9_ALT0` alternate mappings, which allow access to TIM5 and TIM9 respectively. For greater flexibility, allowing us to use more channels per timer, the `HardwareTimer` library or direct port manipulation with the STM32 HAL library, can be used for more detailed control over timer settings [15][19].

2.7 Analog-to-digital converter

An analog-to-digital converter (ADC) is a device that transforms a continuous analog signal into a discrete digital representation that can be then processed by a microprocessor. Fast measurements of analog signals were critical to performing the regulation in due time, mainly when using the current-based compensator, which needs many measurements each cycle.

2.7.1 Analog read

Initially we used the `analogRead` function from the Stm32duino core [19], interfacing the built-in ADC in the microcontroller. This function is easy to use, with support for many microcontroller variants, and does not require

any setting up. Due to this generality, it is also incredibly slow, taking about 48 µs for one measurement.

2.7.2 External ADC

To offload ADC measurements from the main microcontroller and let it focus on control algorithms, we tried adding an external ADC chip, namely the *MCP3008* 10-Bit, 200kSPS, 8-Channel ADC [20]. The ADC communicates with the microcontroller using the SPI protocol, and while providing a theoretical conversion speed of up to 200 kSamples/second, in practical operations with multiple input channels, SPI communication with the STM32 microprocessor was slowing it down, and I could only get to about 40 kSamples/second or 33 µs per measurement.

This was only a small improvement over the first method, yet it also needed a lot of external circuitry, to provide stable power supply and ground to the circuits. This proved to be a weak point of this method, as using the coils generated a lot of interference, for example generating voltage spikes in the power lines.

2.7.3 HAL ADC

The default `analogRead` function is very slow, despite the datasheet [15] claiming the *STM32F411RE* should be able to perform ADC measurements at up to 2.4 Msamples/s. We implemented our own analog read function using the medium-level Hardware Abstraction Layer (HAL) interface provided by STM, allowing us to directly configure and control hardware peripherals.

To read from the ADC using the HAL, the following setup steps are required: first, enable the ADC clock and the GPIO clock for the pin intended for analog input, using the pin's port name and port number. Then configure the GPIO pin as an analog input with no pull-up resistor, and set the ADC speed by adjusting the prescaler, sample time, and resolution. By adjusting these parameters, we balance the time needed for the conversion with the accuracy of the reading. A higher sample time was chosen, in order not to influence the value read from the drivers current sense pin.

For each ADC measurement, the channel is configured using the function `HAL_ADC_ConfigChannel()`, connecting the pin to the microcontrollers ADC using its internal multiplexer. The conversion is then started with `HAL_ADC_Start()`, and the code waits for completion with a blocking timeout using `HAL_ADC_PollForConversion()` . Once the conversion is complete, the ADC result can be read using `HAL_ADC_GetValue()`. After this, the ADC is configured to stop and wait until the next conversion is required [21].

With this approach, the time it took for the ADC conversion dropped to only about 12.4 µs. For further improvements, we could implement reading using direct memory access [21], but this is now fast enough so that the calculations performed take longer than reading the ADC, diminishing the benefits of further speed improvements.

2.8 Control

Using the compensated measurements of the position, we will design a regulator that will make the system stable. The midpoint for the regulation is set manually by feeling the center of magnetic field while moving the levitating magnet above the platform.

We will separate the system into two independent axes of the plane based on the sensor readings and orientation - X and Y. This will be justified using simulations in Section 3.2.2. For each axis, we can use two coils for controlling, which should not influence the position in the other axis. This holds only when the levitating magnet is in the very center of the platform, but the regulation should be able to correct for this error by itself, as the influence is very small. More details on the projection of the force of the coils will be provided in Section 3.2.3.

2.8.1 Experimentally tuning a PID regulator

The PID regulator was initially tuned using an experimental approach by iteratively adjusting the proportional (P), integral (I), and derivative (D) gains based on the observed system stability and the reaction to disturbances.

The tuning process began by gradually increasing the proportional gain to produce a sufficiently strong coil response, perceptible as an opposing force when manually holding the levitating magnet above the platform and moving it in the XY plane. Ideally, in the steady-state position at the central point, the magnet should be supported solely by the permanent magnets, theoretically eliminating the need for integral action. However, due to mechanical imprecisions, play in the platform components, and non-linear effects such as core hysteresis, a consistent central equilibrium point could not be reliably identified. To enable steady-state actuation of the coils, an integral component was introduced, resulting in a system that achieved near-stable levitation. Nevertheless, the system exhibited a poor response to disturbances, primarily due to insufficient intrinsic damping, and began to oscillate. During quick magnet movements, control loop performance deteriorated, probably as a result of increased compensator error. To address this, derivative gain was added to improve damping of the system, allowing the levitating magnet to return to steady state more rapidly following disturbances.

However, it was observed that increasing the derivative gain beyond a low threshold led to system instability. This behavior was attributed to higher-frequency noise present in the position measurements from the sensor, which the derivative term amplified. As a result, it was necessary to select a relatively low D constant to preserve system stability. This insufficient damping, in combination with generally noisier sensor reading caused by the coil effects on the sensor, manifested itself as some visible oscillations in the levitated object's motion and also audible noise from the coils.

To reduce the noise and allow for higher D constant and damping, we have added a low-pass filter before the regulator. This helped to reduce the rare

but abrupt oscillations caused by spikes in voltage readings. A more efficient solution would be to move the entire hardware setup to a printed circuit board, eliminating the unreliable jumper wires.

2.8.2 Stable levitation

With this PID regulation the magnet would stably levitate above the platform. Before each use, the compensators would need to be tuned again, which was performed automatically, while the magnet was placed steadily above the platform at a levitation height of about 2 cm using a 3D printed holder. Using the current-based compensator with improved ADC reading techniques described in the previous sections greatly increased the levitation time, reducing oscillations and regulation effort.

2.8.3 Automatic midpoint finder

During testing, we observed significant coil actuation even in steady state, causing coil heating, which limited the device runtime. This indicated that the magnet was not positioned at an optimal equilibrium point where minimal support by the coil would be required. To address this, we attempted to dynamically find a more suitable central position where coil intervention was minimized. After achieving initial stabilization of the magnet, an automated procedure was implemented to monitor coil actuation and iteratively adjust the midpoint position used for the PID control in the direction of coil actuation, which should point to the center of magnetic fields. With this approach, we were able to more precisely locate the point of equilibrium, thus significantly decreasing power consumption of the coils. As a result, the platform could maintain levitation for extended periods, effectively enabling near-continuous operation without the need for active cooling of the coils.

Chapter 3

Modeling

We will model our levitation platform in order to get better insight into the working principles, derive transfer function of the system, and allow for designing better control algorithms. Furthermore, it will allow us to experiment with the system to develop more advanced functionalities like rotation control or design different platform configurations. The model will also allow us to verify some of the equations and claims postulated in the previous chapter about the effect of coils and magnets.

For the modeling, we choose the COMSOL Multiphysics software with AC/DC module, which features the Magnetic Fields interface, allowing for the modeling of permanent magnets and currents in coils in electromagnetic problems. The core of electromagnetic analysis at the macroscopic level lies in solving Maxwell's equations, which govern the behavior of electric and magnetic fields in space and time. These equations are numerically solved using the finite element method (FEM), which allows accurate modeling of complex geometries and field distributions [18].

3.1 Finite element method modeling

The model includes electromagnets and permanent magnets in the base with attaching screws and a cylindrical permanent magnet placed at a variable height h in open air. All nonmagnetic, nonconductive components such as plastic or wooden parts are omitted from the simulation because their relative magnetic permeability and conductivity are very close to those of air and their influence on the magnetic field is negligible.

The physical model is enclosed within a spherical domain of radius 60 mm, which is sufficient to encompass the entire levitation platform, where the magnetic fields will be calculated. To accurately model the behavior of magnetic fields extending into free space, the outer boundary of the sphere is layered with infinite element domains. These boundary layers simulate an unbounded air region, ensuring that the truncation of the domain does not influence the results.

Once the geometry is defined, it is discretized into finite elements by meshing the domain with tetrahedral elements. The finite element method (FEM) approximates the solution of Maxwell's equations by solving them

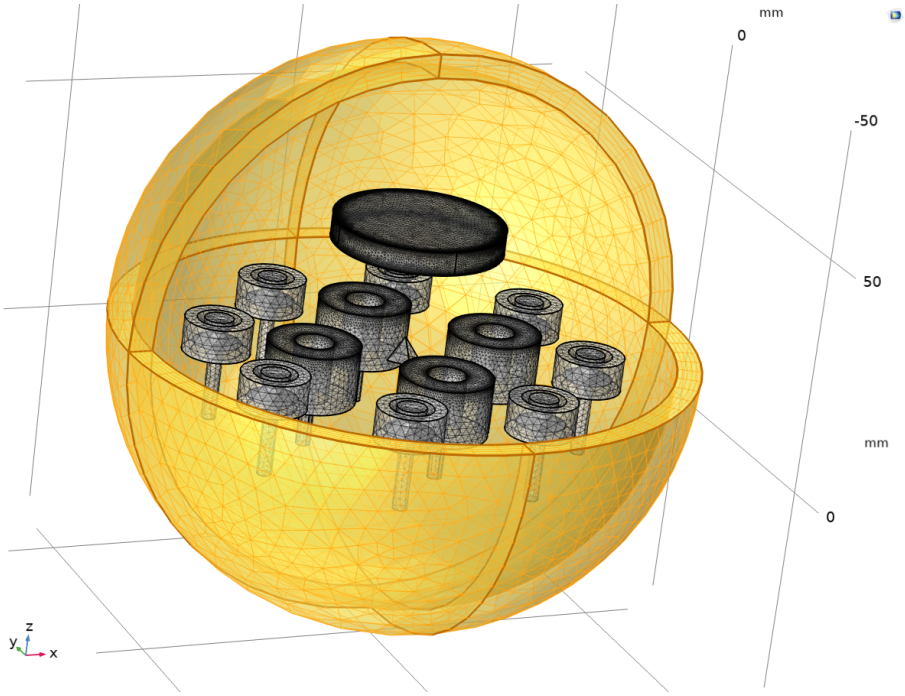


Figure 3.1: Meshing of the platform in COMSOL FEM, with infinite domain in yellow. The pyramid in the center acts as point positions of the Hall effect sensors.

locally within each element. The mesh density needs to be chosen on the basis of the expected field gradients and required solution accuracy. Finer meshes are used in regions with steep field variations to improve numerical precision without excessive computational cost [22][18].

3.1.1 Force calculation

To calculate the magnetic forces that act on the levitating permanent magnet, COMSOL uses the Maxwell Stress Tensor method, evaluating the stress exerted on the body by the surrounding magnetic field. The force is obtained by integrating the stress tensor at the boundary surface of the magnet

$$\vec{F} = \oint_S \vec{n} T \cdot dS, \tag{3.1}$$

where $\vec{F}$ is the total force on the object, T is the stress tensor of the outer domain (air) and $\vec{n}$ is the normal pointing outward from the surface.

The Maxwell stress tensor for electromagnetic stationary fields in vacuum or air is given by

$$\mathbf{T} = \epsilon_0 \left(\mathbf{E}\mathbf{E}^T - \frac{1}{2} E^2 \mathbf{I} \right) + \frac{1}{\mu_0} \left(\mathbf{B}\mathbf{B}^T - \frac{1}{2} B^2 \mathbf{I} \right), \tag{3.2}$$

where ϵ_0 and μ_0 are the vacuum permittivity and permeability, $\mathbf{E}$ and $\mathbf{B}$ are the electric and magnetic field vectors, and $\mathbf{I}$ is the identity matrix [18].

In practice, this method proved to be numerically sensitive. The computed force values showed significant variation depending on the density of the mesh, particularly around the sharp edges of the magnets.

3.1.2 Meshing

To improve reliability, we implemented an iterative mesh refinement strategy in which the mesh was progressively refined and the resulting force values were tracked. This allowed us to study convergence behavior and determine the mesh resolution required to achieve consistent results, which was then used for all other calculations. The mesh was most refined around the levitating magnet, particularly near its sharp edges, which are problematic for force calculations [22]. In these regions, the maximum element size was set to 0.16 mm, increasing up to 0.8 mm on the flat surfaces of the magnet.

To improve element quality and avoid skewing near corners, a single boundary layer of 0.1 mm thickness was added around the magnet. This helped smooth the transition between the magnet surface and the surrounding air domain.

For other parts of the model, such as the base magnets, coils, and surrounding air, a coarser mesh was sufficient. Due to the relatively large distances and weaker gradients in these regions, further refinement did not improve accuracy as much, while leading to longer computation time. Furthermore, a reduced element growth rate of 1.25 was used throughout the air domain to maintain higher mesh density around the refined bodies, while allowing coarser elements in regions farther away to reduce the total number of elements.

3.1.3 Modeling the magnets

Accurate representation of the components was essential to obtain realistic force predictions from the FEM model. The magnet model was redesigned several times and verified against experimental data to improve the accuracy of the simulation. In particular, we compared the computed vertical magnetic force (z-axis) with the force required to support the levitating body, which weighs 63 g.

Magnets were modeled using the Remanent Flux Density formulation within the Ampère's Law interface. This approach allows for the definition of permanent magnets via a normalized magnetization direction vector, with the remanent flux density magnitude determined by the material properties.

Initially, the base magnets were modeled as simple hollow cylinders, representing the entire stack of three magnets from Figure 4.2. However, this led to an overestimation of the magnetic lifting force. We tried to improve on the model by representing the individual three magnets magnets that make it up, including fillets around their holes to reflect the actual shape. Surprisingly, this adjustment resulted in only minor improvements.

A key change was when we also added the iron screw that holds the magnet stack together, to the model. Including it significantly affected the magnetic field distribution and, consequently, the computed z-axis force. With this

addition, the simulated forces dropped considerably, reaching values much more consistent with the real-world measurements.

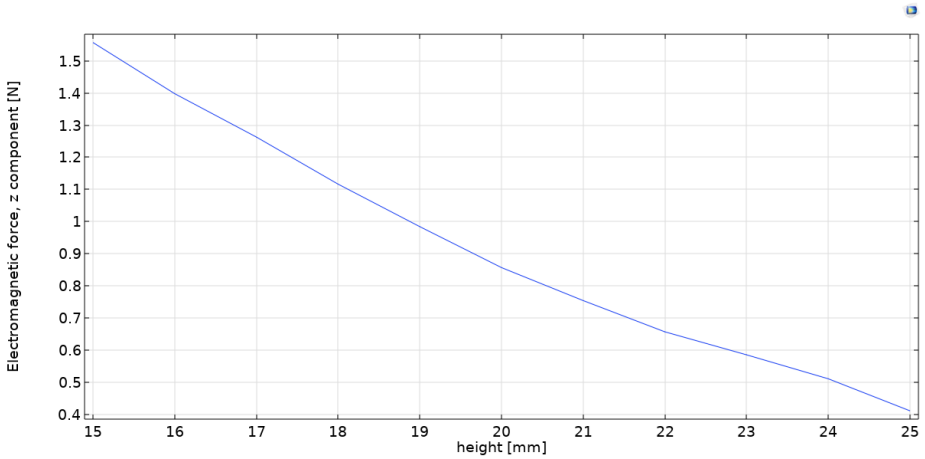


Figure 3.2: Modeled lifting force of the passive magnet for various heights of the magnet. At $F = 0.63$ N, the magnet weight should be supported.

The magnet height was measured with coordinate $z = 0$ set to the bottom edge of the magnet touching the top edge of the coils.

3.1.4 Modeling the coils

The electromagnetic coils were modeled in COMSOL using the homogenized multiturn Coil feature, allowing for efficient simulation of tightly wound wire coils by treating them as a continuous domain with uniform current density. Each coil was defined as a 500-turn winding using AWG 28 copper wire, in accordance with the parameters listed in Table 2.1.

Two configurations were investigated: one with ferromagnetic cores (soft iron material with simulated B-H curve) and one with air cores. This allowed us to assess the impact of the cores on the forces produced by the coils. In line with the treatment of the base magnets, the screws used to secure the coils were also included in the model, as they were found to influence the magnetic field in the surrounding region.

To validate the coil models, we compared the simulated magnetic flux density, available in Appendix A.6 and A.7, at the levitation height with experimental measurements from Figure 2.14. Comparisons were made for both core variants, and the results fit with the shape, but the simulated magnetic induction is about 10 % away from the measured values. This may be caused by different material properties (for example of the cores) or as slightly shifted position of the magnetometer, as the gradient of the magnetic field are steep around the center.

3.2 Results

3.2.1 Sensors readings

We will verify Equation 2.4 relating sensor readings to positional displacement. Using the computed magnetic fields at the position of each of the Hall sensors, we computed the reading from the sensors for each position of the levitating magnet. The results of this are visible in Figure 3.3 below.

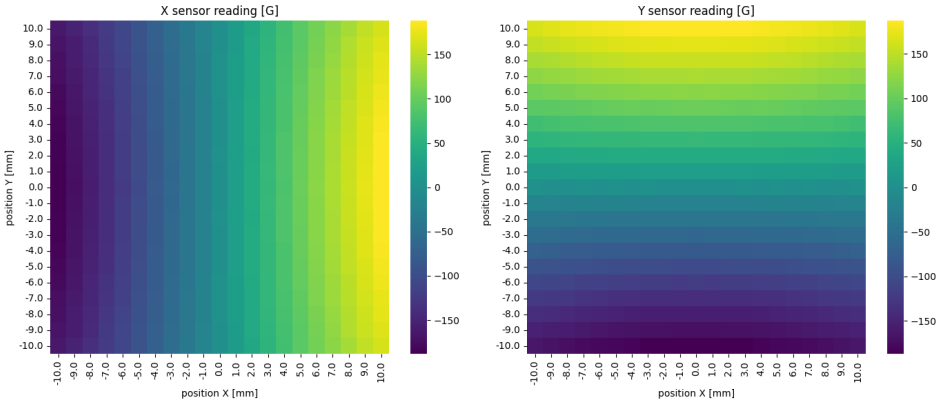


Figure 3.3: Simulated sensor readings for various positions measured from the center.

We tried to fit the known positions with the simulated sensor reading with linear and quadratic function, with the constant coefficient set to zero. With the linear function, we managed to get a fit with a R^2 factor of 0.997, where only the respective axes were used (the position x depended only on the measurement on the x-axis). Using the quadratic function yielded no improvement at all.

$$x = 0.0533\frac{mm}{G} \cdot B_{sens\_x} + 0 \cdot B_{sens\_y} \tag{3.3}$$

$$y = 0.0534\frac{mm}{G} \cdot B_{sens\_y} + 0 \cdot B_{sens\_x} \tag{3.4}$$

As those coefficients should in theory be the same and the difference is caused by numerical errors of the FEM solver, in the actual code we used an average value. It just had to be adjusted considering the sensitivity of the Hall sensors multiplied by the OP AMP to 14 mV/Gauss [1] and ADC sensitivity of 3.23 mV/LSB:

$$x = k_{pos} \cdot (U_{sens\_x} - U_{ref}), \tag{3.5}$$

$$y = k_{pos} \cdot (U_{sens\_y} - U_{ref}), \tag{3.6}$$

where $k_{pos} = 0.0533\frac{mm}{G}/14\frac{\text{mV}}{\text{Gauss}} \cdot 3.23\frac{\text{mV}}{\text{LSB}} = 1.23 \cdot 10^{-2}\frac{mV}{Gauss}$, U_{sens_x} and U_{sens_y} are voltage readings from the sensor and U_{ref} the sensor reference

voltage. This matches the theoretical results obtained from Equation 2.4 earlier, that the sensor readings in the x-axis depend only on the x position of the magnet, while close to the center.

3.2.2 Transfer function of the platform

Measuring force of magnets

To develop a transfer function for the magnetic levitation system, we began by measuring the modeled magnetic forces generated by the permanent magnets at different positions of the levitating magnet. In the horizontal XY plane, the force was fitted with a linear function, the farther the object moves away from the center, the stronger the magnetic force becomes in the same direction. This is unstable behavior, as the force will increase as the object moves outward, pushing it further away, as visible in Figure 3.4.

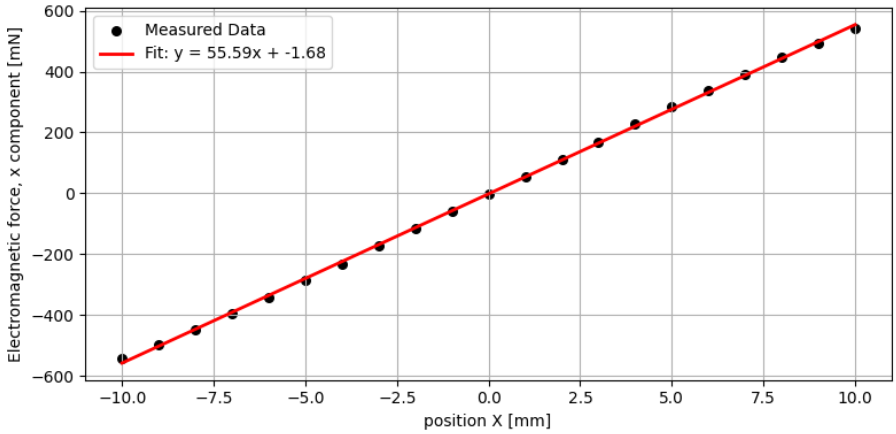


Figure 3.4: Measured force in the XY planes for various distances of the magnet from the center, with linear fit.

For the z-axis force, we used a quadratic function to model the decreasing upward force as we move off the center. These functions seem to fit the data well, while being simple enough for analysis. The results of the fitting are shown below in Figure 3.5.

Deriving transfer function

The magnetic force acting on the levitating magnet in the XY plane is approximated near the equilibrium point by linear fit

$$m\ddot{\vec{r}} = F_{mag}(x) = k\vec{r} \tag{3.7}$$

where $k = 55.6$ N/m is the experimentally determined coefficient. We can neglect the constant factor, as it is small compared to the linear coefficient and likely due to numeric errors in the simulation.

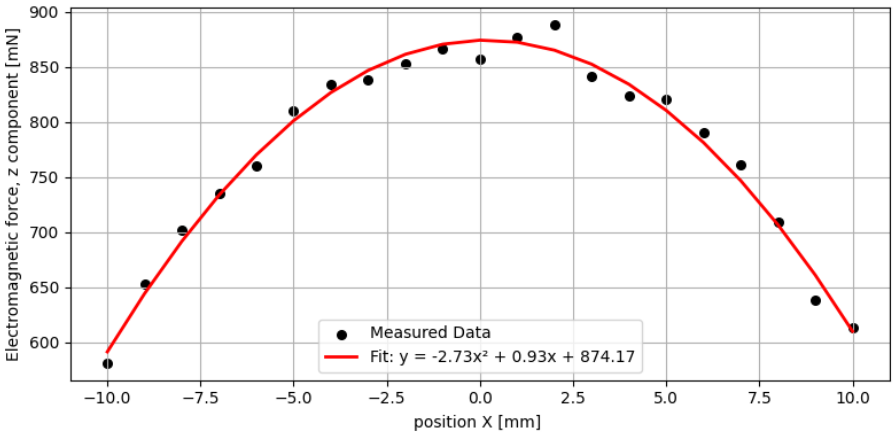


Figure 3.5: Measured force in the z-axis for various distances of the magnet from the center, with quadratic fit.

An important observation is that this equation is separable into two positional components. This allows us to rewrite the vector equation as scalars and also perform all the control separately, rather than as a multiple input-multiple output system. By including also the regulation force projected on the magnet by the coils, we add another term to this equation

$$m\ddot{x} = kx + F_{x\_coils}\,. \tag{3.8}$$

Applying the Laplace transform on this differential equation gives

$$ms^2X(s) = kX(s) + F(s)\,, \tag{3.9}$$

where $F(s)$ represents the input to the system from the coils. This leads to the system transfer function

$$G(s) = \frac{X(s)}{F(s)} = \frac{1}{ms^2 - k}\,, \tag{3.10}$$

which is a transfer function of a unstable system, with one pole in the positive half-plane.

Regulator design

In previous chapter, we have experimentally tuned a PD regulator for the platform. Now we will theoretically verify our findings, showing that PD is the minimal regulator needed to stabilize the system and give constraints on the parameters of the regulator.

The equation for PD regulator in the Laplace domain is

$$R(s) = K_p + K_d s\,. \tag{3.11}$$

The closed-loop transfer function of the whole platform, combining Equation 3.10 with the regulator from Equation 3.11, is

$$H(s) = \frac{K_p + K_d s}{ms^2 + K_d s + (K_p - k)}\,. \tag{3.12}$$

The poles of the system are the roots of the denominator

$$s = \frac{-K_d \pm \sqrt{K_d^2 + 4m(k - K_p)}}{2m}\,. \tag{3.13}$$

For stability, the real parts of the poles must be negative. This is ensured when

$$K_d > 0 \tag{3.14}$$
$$K_p > k\,. \tag{3.15}$$

With a P regulator, we could get the poles arbitrarily close together, but we cannot reach stability. Only after introducing $K_d > 0$, the system stabilizes.

3.2.3 Force field of coils

In order to verify the force model and fit the constants, we will simulate the forces projected on the levitating magnet by a coil placed at position $y = -20$ mm carrying $I = 1$ A of current, for various positions of the magnets, sweeping from -10 mm to 10 mm in both axes independently. For this measurement, we used a model of coils with no core, as this variant will be used in the following chapters. Using the equations derived previously in Section 2.4.5 we will try to fit Equation 2.16 with the distance and height of the theoretical magnetic charge inside the coil and also the scaling constant k_{coil}. The equation describes all three axes components of the force. We were unable to find a good fit for all components at once, with the z-component identified as the outlier. We will discuss the z-axis force in more detail in Section 4.2. For determining the XY components of the force, we fit our simulated data with equation

$$\vec{F}_{xy} = I k_{force} \frac{(x, y - y_0)}{[x^2 + (y - y_0)^2 + (z - z_0)]^{5/2}}\,. \tag{3.16}$$

The results of the fit with the values for constant $k_{force} = -2680 \frac{\mathrm{N \cdot mm^4}}{\mathrm{A}}$, distance $y_0 = -14.3$ mm from the center and height $z_0 = -9.5$ mm from the top of the coils are in Figure 3.6.

Using these fitted functions, we can better estimate the force projected on the magnet by the coils, enabling for more accurate control.

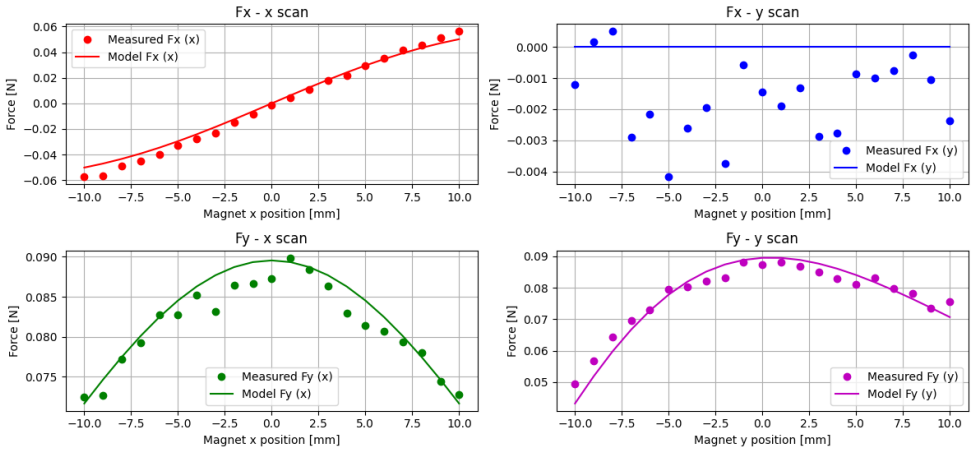


Figure 3.6: Measured force of a coil at $y = -20$ mm from the center carrying 1 A of current, for various positions of the magnet, fitted with the derived theoretical force function.

Chapter 4

Elevation and rotation

In this chapter, we implement control over the elevation and rotation of the levitating magnet. We will test different configurations and the number of magnets and coils in the platform to allow more precise and energy-efficient control over the levitating magnet.

To develop these improvements more quickly, the magnetic levitation platform was transformed into a modular set of parts that can be toollessly arranged in any pattern. The code was redesigned to allow easy identification of different coil placements and numbers. More individual and precise control over the coils was needed in order to control the rotation and height of the magnet, without disturbing the **XY** position of the magnet controlled by the PID controller described in the previous chapter.

4.1 Modular set

We created a modular blocks out of the Hall effect sensor module, electromagnetic coils, and permanent magnets. They were designed in such a way that they can be placed between two plates that would rigidly fix their position with a gap of 5 mm for routing cables. To allow for rapid and inexpensive prototyping, a laser cutter was used to manufacture the supporting plates from plywood sheets.

4.1.1 Parts

Magnets

The magnets described and depicted in Figure 2.7 were fixed onto a 3D printed piece with a metal screw that was screwed into a heat-set insert nut counterpart. The height of the module was chosen so that the magnets matched the upper edge of the coils. The module alongside with its Fusion 360 model is visible below in Figure 4.2.

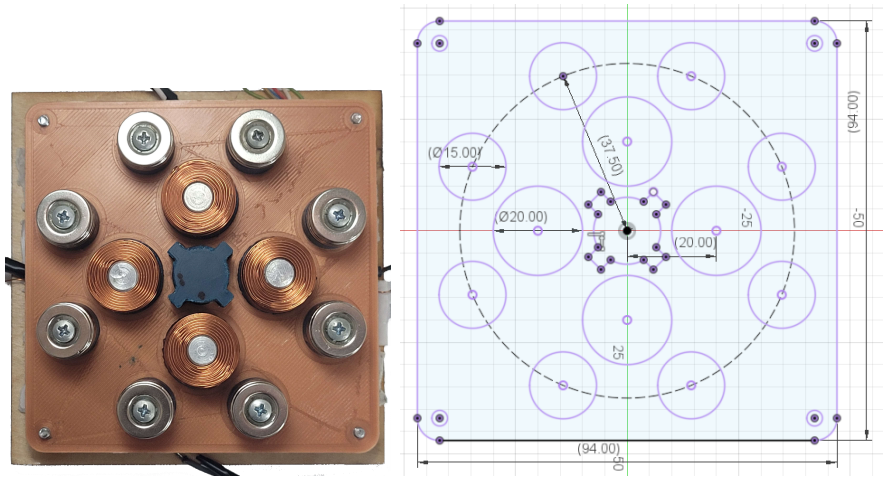


Figure 4.1: Modular set used to build the default 4-coil platform design alongside with a drawing with dimensions.



Figure 4.2: Magnet piece from the modular set with its Fusion model on the right.

Coils

The coil modular piece combines the electromagnetic coils from Figure 2.6 with a *B3435* 10 kΩ thermistor fixed directly under the coil in the small ring section to one side of the module. To improve measurements of the temperature, we used heat-conducting paste. Both the coil and the thermistors were connected to an extension cable that ends with a 4-pin connector. The 3D model of this part and its physical appearance can be seen in Figure 4.3.

Coil driver

The whole coil module can be connected to a custom-built module for *DRV8874* POLULU driver board. This module allows for the configuration of the driver board for *Phase*, *Phase/Enable* or *Vref* modes as described in Section 2.4.1 using jumpers placed over the various pins of the module. Using these modules reduces the number of cables needed to interface the drivers and simplifies the connection of the coils. Improperly connected or

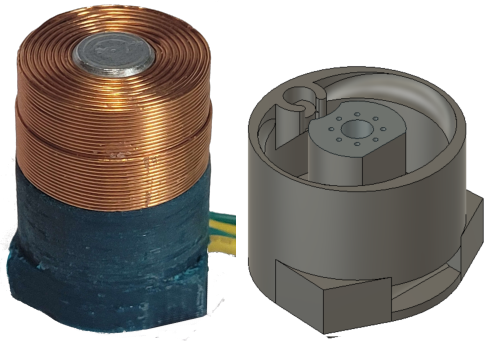


Figure 4.3: Coil piece from the modular set with its Fusion model on the right.

accidentally disconnected cables can cause damage or destruction of sensitive components such as drivers or the microcontroller, particularly given the relatively high operating voltages of up to 24 V.

The coil module includes an LED for the indication of coil overheating, which lights up when the thermistor resistance drops. A variant with two connectors for connecting two coils in antiparallel orientation was also developed, which simplified control requirements for some cases.

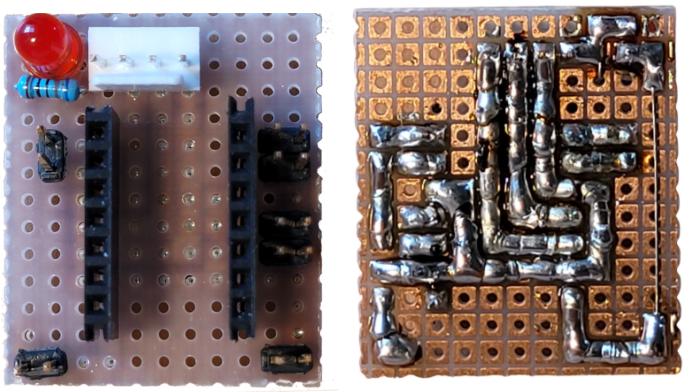


Figure 4.4: Coil driver module with connector for coils (White), socket for the *DRV8874* POLULU driver (Black), LED overheating indicator and pins for configuration and connection to a microcontroller, view from top and bottom.

4.2 Elevation control

In this section, we develop control over the elevation of the levitating body. In order to control and regulate the position of the magnet in the z-axis, we have to add a sensor to perform height measurement. With changing height, sensor measurements have to be adapted, as the magnetic field diminishes with increasing height, influencing readings from planar Hall effect sensors. This will also be useful if a heavier object is levitated, as the height of the levitation depends on the weight of the object as shown in Figure 3.2. Lastly,

we will investigate how the varying height influences the force projected on the magnet and if this influences the control algorithm used in the XY plane.

4.2.1 Principles

The vertical position of the levitating magnet is controlled by actuating all coils simultaneously with equal current direction and magnitude. This actuation will be added on top of the controller that stabilizes the magnet in the XY plane and has to be designed in such a way to not disturb the regulating algorithm.

4.2.2 Individual coil control

Elevation control over the levitating magnet requires the ability to actuate each coil individually, not in pairs, as previously performed. However, experiments revealed that this makes control and compensation of the coil effects much harder. While actuating the coils in antiparallel pairs, most of the negative effects of the coils on the sensors seemed to cancel out. Most significantly, the ferromagnetic core remained magnetized even when no current was flowing through the coil, which affected the sensors in a way that we could not adequately compensate.

To address this, the ferromagnetic core was removed from the coil and replaced with a plastic counterpart that would hold the coil down. This significantly improved linearity in coil effects, with a little bit of hysteresis remaining due to a metal screw holding the coil. In this configuration, the current-based compensator proved to be highly effective, allowing the nullification of most of the effects, despite controlling the coils separately. Another effect of this modification was the electrical characteristics of the coil also changed: the inductance dropped to approximately 2 mH, and the time constant was reduced to around 0.4 ms. A downside of this modification is the reduction of the force projected by the coil on the levitating magnet by about 50 %, as determined by FEM simulations.

4.2.3 Simple height control

When all coils are actuated in unison by a constant offset added to the positional regulator, the magnet's vertical position can be adjusted slightly - within a range of about 2 mm in either direction from the equilibrium point, as shown in the image in Figure 4.5. However, the damping of the system is very small, requiring up to a minute for the magnet to settle.

4.2.4 Height measurements

To allow active regulation of the vertical position of the levitating object, an additional Hall effect sensor was added to the system and oriented along the z-axis. This sensor allows for direct measurement of the magnet's elevation above the platform, allowing for closed-loop feedback control. As with

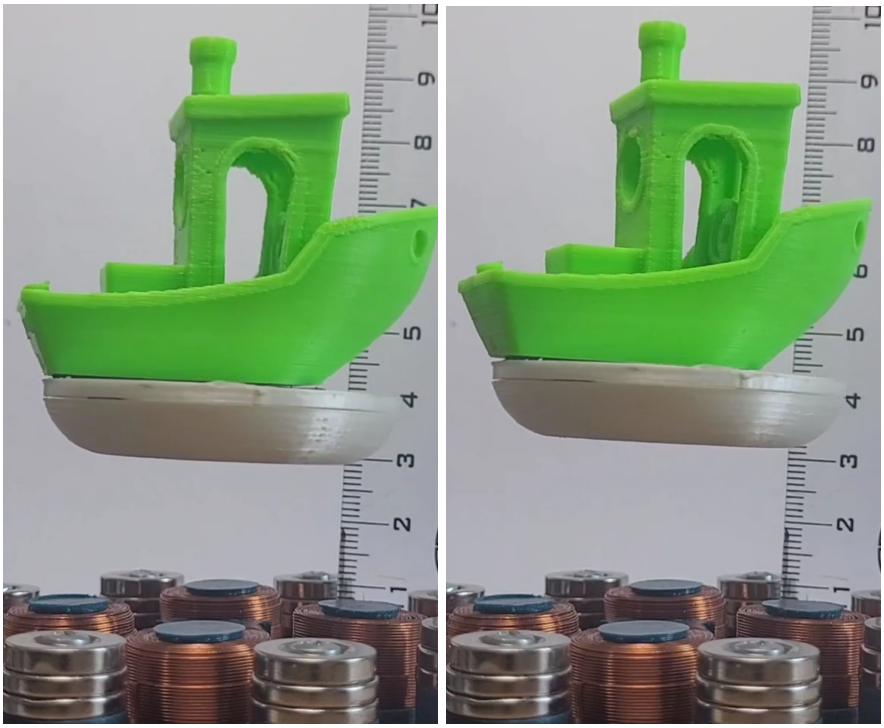


Figure 4.5: Height control of the levitating object.

other sensors, the z-axis sensor experienced interference from coil-generated magnetic fields. By adapting the current-based compensator, this effect was successfully mitigated, resulting in accurate position measurements.

In order to transform the sensor readings, we will once again try to fit the measurements with the theoretical Equation 2.1:

$$\vec{B} = \frac{\mu_0}{4\pi}\left(\frac{3\vec{r}(\vec{m}\cdot\vec{r})}{r^5} - \frac{\vec{m}}{r^3}\right). \tag{4.1}$$

By considering magnetic induction only in the z-axis directly above the sensor, we can simplify as

$$\vec{B}_z = \frac{2\mu_0 m}{4\pi}\frac{1}{h^3} = k_{height}\frac{1}{h^3}. \tag{4.2}$$

We were unable to find a fit of the equation with the data gathered from the simulations of the sensor measurements. This is likely due to the fact that the dipole equation assumes a magnetic dipole of negligible size, whereas our magnet dimensions are considerable in comparison to the distances.

After fitting the function with the power function, we have determined that the data fits best with $B_z = k\frac{1}{(h+2.5\text{ mm})^{1.75}}$ with RMSE of 0.25 mm. The inversion of this function is slow to implement on the microcontroller, so we instead opted for choosing a slightly worse fit with $B_z = k\frac{1}{(h+2.5\text{ mm})^2}$ with RMSE of 0.37 mm. The offset of 2.5 mm is due to the height being referenced to the bottom edge of the magnet, with the middle at 2.5 mm from the edge. Both of these fits are visible below in Figure 4.6.

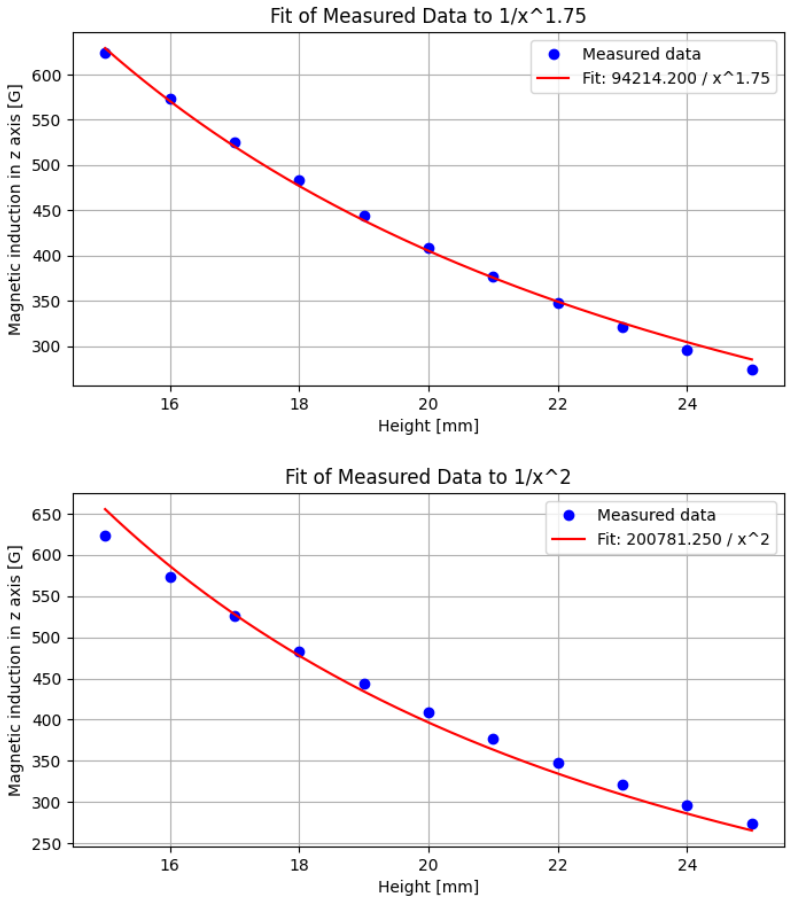


Figure 4.6: Magnetic induction in relationship with height of the levitating magnet, fitted with power and quadratic functions.

By inverting this function, with $k = 2 \cdot 10^5$ G mm^2 we can calculate the horizontal distance of the center magnet as

$$h = \sqrt{\frac{k}{B_z}} - 2.5 \text{ mm}\,. \tag{4.3}$$

Calculating the square root of a float is much faster on the microcontroller than a general power function, since the Floating-point unit (FPU) of the STM microcontroller implements this in hardware with the *VSQRT* instruction [23].

4.2.5 Sensor readings in relation to height

The magnetic induction values measured by the position sensors in the XY plane decrease as the levitating magnet moves higher. To account for this, we need to scale the sensor readings based on the height of the magnet. As discussed in Section 4.2.4, accurately modeling the relationship between magnetic induction and height is not straightforward. However, by analyzing

the data, we can closely match the drop in position sensor values with the corresponding measurements from the height sensor. Comparisons of the sensors for two different positions of the magnet are displayed in Figure 4.7.

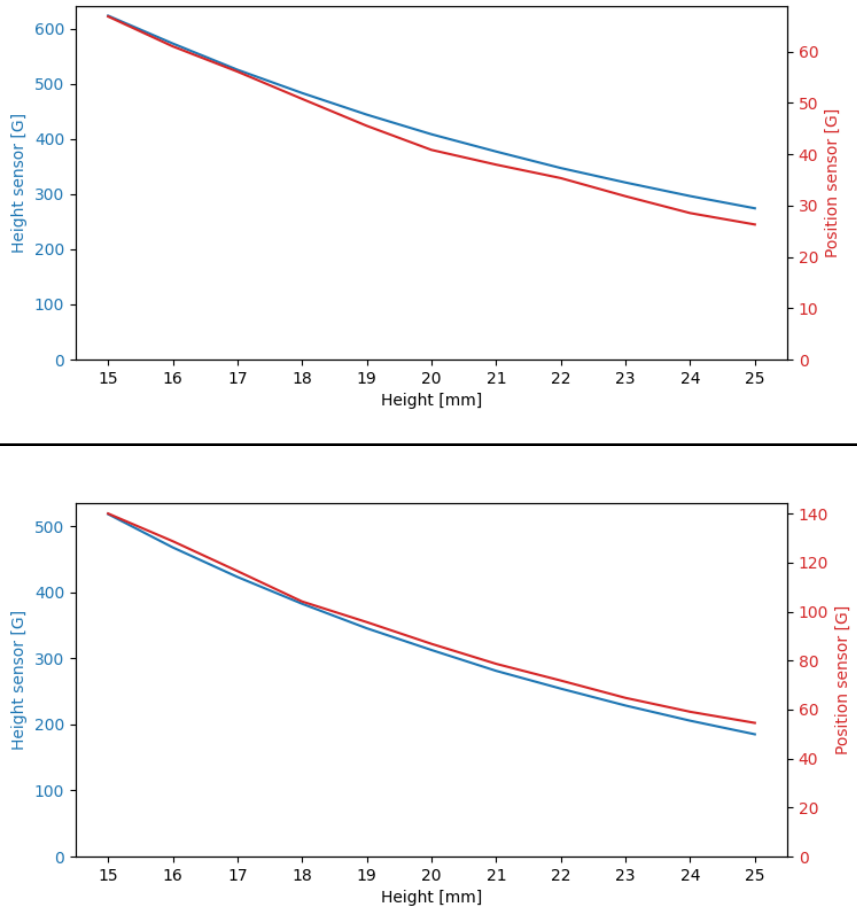


Figure 4.7: Comparison of height and positional sensor readings with varying height.
Top: magnet at the midpoint, Bottom: magnet displaced to $y = 5$ mm from the midpoint.

Therefore, we scaled the position sensor readings by dividing them by the relative change observed in the height sensor, which leads to improvement over Equation 3.6:

$$x = k_{pos} \cdot (U_{sens\_x} - U_{ref}) \cdot \frac{B_{z0}}{B_z}\,, \tag{4.4}$$

$$y = k_{pos} \cdot (U_{sens\_y} - U_{ref}) \cdot \frac{B_{z0}}{B_z}\,. \tag{4.5}$$

Using these equations, we can obtain more accurate positional readings independent of the height of the levitating magnet.

4.2.6 Forces with relation to height

Next we analyzed the forces acting on the system in the XY plane to observe how they change with height and whether an adjustment of the regulator is necessary. From the simulation, we found that both the passive radial force of the magnets, pushing the magnet off center, and the active force generated by the coils decrease as the magnet rises. This is in line with the predictions given by Equation 3.16 for the force of coils that was derived in the previous chapter, with the prediction in Appendix A.8.

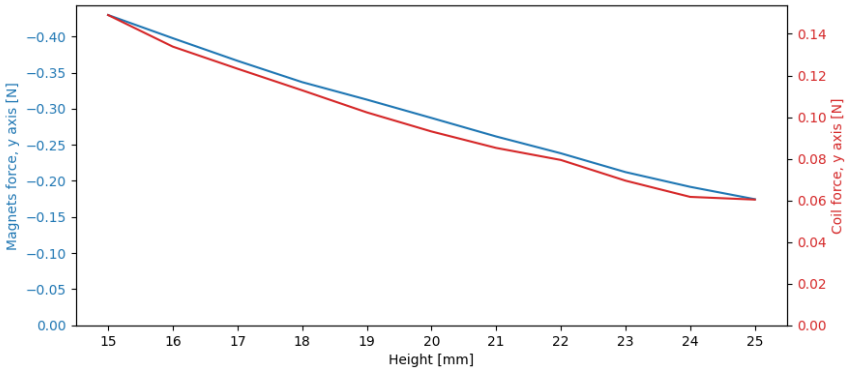


Figure 4.8: Comparison of radial force form magnets and force of one coil running at $I = 1$ A at $y = -20$ mm with the magnet at $y = -5$mm.

From the results shown in Figure 4.8, both forces drop proportionally to height. Referring to Equation 3.8, both the passive force of the magnets $F_{magnets} = kx$ and the coil-generated force $F_{\text{coils}} = (K_p + K_d s)E(s)$ decrease by the same fraction, $f_F(h)$. This implies that the total force acting on the magnet, $F = m\ddot{x}$, is also reduced by the same proportion, but with its sign unchanged. The transfer function of the system, considering the changing height, will be as follows:

$$H(s) = \frac{f_F(h)K_p + f_F(h)K_d s}{ms^2 + f_F(h)K_d s + (K_p - k)f_F(h)} = \frac{K_p + K_d s}{\frac{m}{f_F(h)}s^2 + K_d s + (K_p - k)}, \tag{4.6}$$

which leads to the poles of the system placed at

$$s = f_F(h)\frac{-K_d \pm \sqrt{K_d^2 + 4m(k - K_p)/f_F(h)}}{2m}. \tag{4.7}$$

The constraint on system stability $K_p > k$ and $K_d > 0$ will remain unchanged. However, the poles will be closer or further away from zero, scaled by the height-dependent positive function $f_F(h)$. As a result, the system remains stable using the same regulator parameters, but the swiftness of response will change.

4.2.7 Height regulation

With reliable height measurements, a derivative (D) controller was implemented to stabilize the vertical motion of the magnet and reduce oscillations. In particular, the addition of the derivative term served to introduce damping into the system. This was beneficial for stabilizing the magnet, even without any height adjustment, as the inherently low mechanical damping in magnetic levitation systems makes them especially susceptible to long oscillations.

The comparison of the magnet height response to a Dirac impulse is shown in Figure 4.9. Without any regulation, the magnet oscillates and takes almost 20 s (outside of the graph) to settle back into steady state. On the other hand, with the moderately tuned D regulator at $K_d = 0.05$, the system stabilizes in about 2.5 s. With higher K_d we obtained even faster results, but at the cost of increased power consumption and occasional noise-induced oscillations.

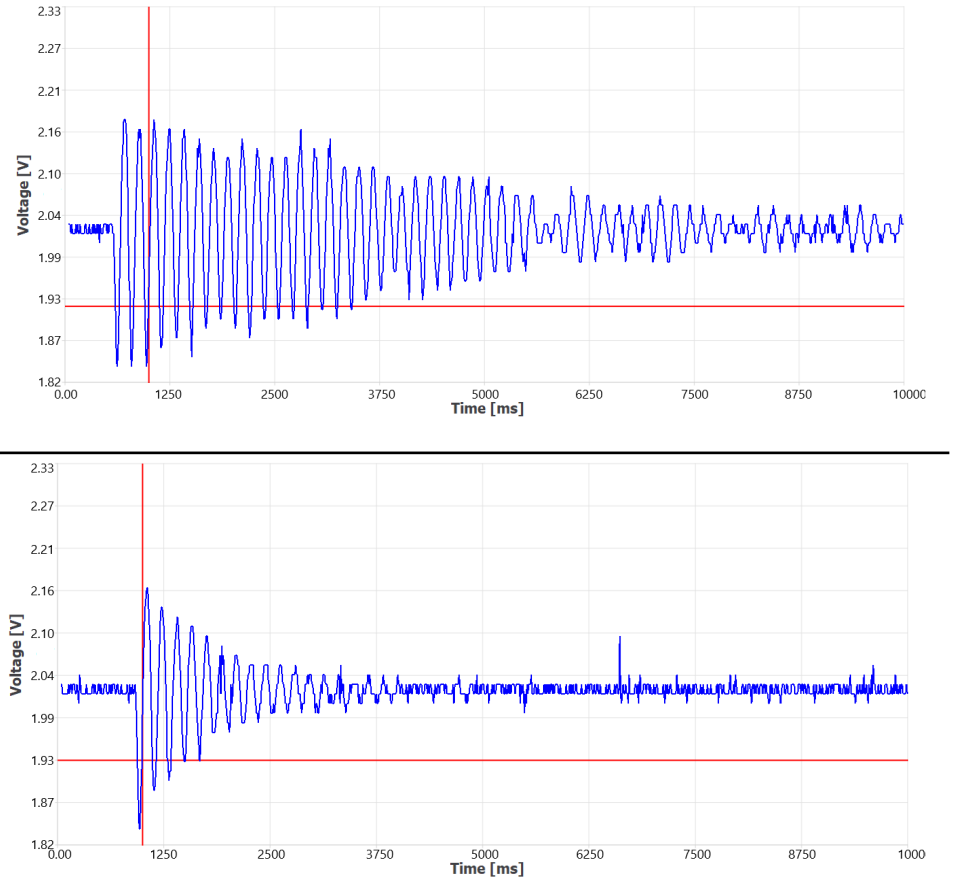


Figure 4.9: Effect of D regulator damping on oscillations in height. Top: undamped system, Bottom: system damped with D regulator.

4.2.8 Lifting force of coils

Modeling of the electromagnetic force in the z-axis with the finite element method proved to be tricky, the results varied a lot with different coil geome-

tries and were not consistent, when modeling only a single coil at a time. We have thus modeled turning all the coils at once, as described in Section 4.2.3. The force projected by the four coils, running 1 A of the current, is shown in Figure 4.10.

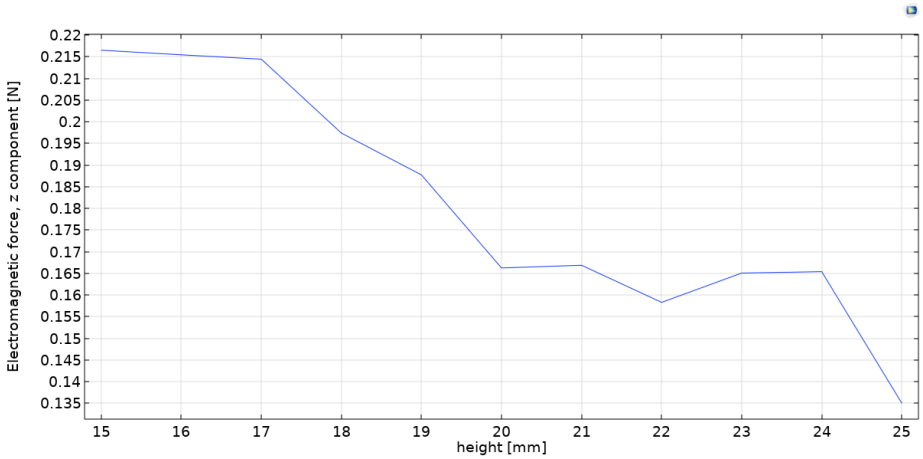


Figure 4.10: Force projected on the magnet in z-axis depending on its height, using four coils with each running 1 A of current.

The numerical instability is visible in the results, but they can still be used to deduce the maximal feasible height adjustment. Looking at the lifting force of the magnets from Figure 3.2, we see that we loose about 0.13 N of force per millimeter of elevation, while the coils are capable of providing less than 0.2 N of lifting force, depending on the height. This shows that we will be able to change the height approximately in the range of about ± 2 mm, consistent with the results obtained in Section 4.2.3.

4.3 Platform arrangements

Using the developed modular set, we experimented with various arrangements of the magnets and coils around the platform to allow for varied applications. For analyzing the coil and magnet arrangement, we will use data experimentally found in the previous chapters.

Looking at the graphs in Figure 3.6, one interesting conclusion is that the initial distance of 20 mm of the coils from the center is optimal for exercising maximal radial force on the magnet ('Fy - y scan' graph). The force decreases if we move the coils farther, but only slightly, but moving them closer, the force drops radically.

4.3.1 6-coils arrangements

By moving the coils slightly farther away, we can make room for more coils, leading to a 6-coil arrangement as in Figure 4.11. By increasing the number of magnets to 12 from the initial 8, we can allow for levitating even of heavier

objects. It was found that with this many magnets, for a light object such as the plastic boat used initially, as visible in Figure 2.1, the object is too high above the coils, rendering them inefficient and the levitation was not very stable. By removing half of the coils, we can make the object levitate closer to the base, allowing for stronger coil effect.

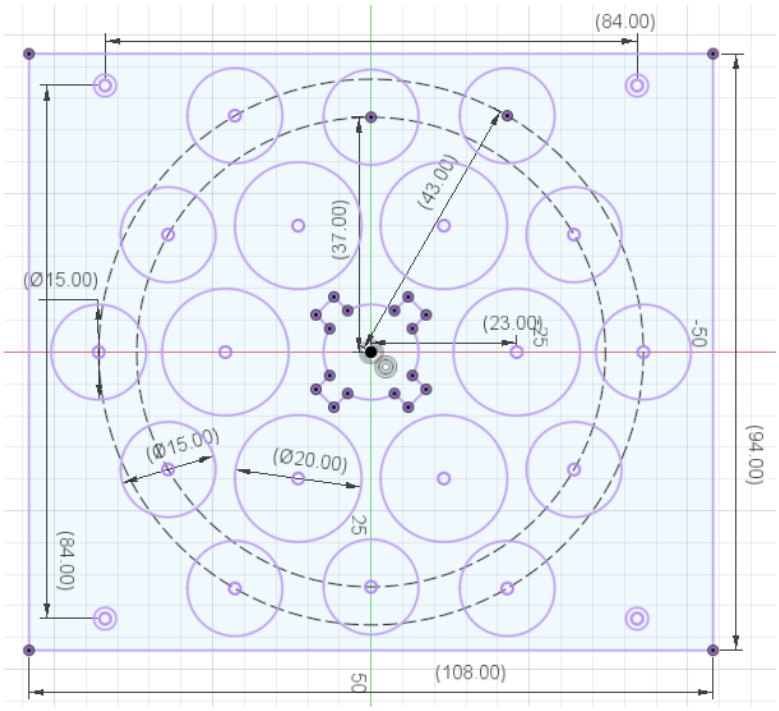


Figure 4.11: A drawing with dimensions of the base used to build a 6-coil platform.

4.3.2 Lateral forces

The lateral forces (forces in the XY plane) exerted by the coils reach 0.18 N if two coils are used at once in a 4-coil setup. With a 6-coil setup, we can increase this force up to 0.32 N, when using all the coils at once. These calculations assume 1 A of the current running in the coils, which seems to be the maximum current that can be sustained for some time, before the coils start overheating. Also, as the current is distributed into more coils, we can exercise the same force but with less heat generated than in the 4 coils design, since the generated heat scales with current squared. This indicates that a 6 coils is beneficial for applications requiring more lateral strength. The redundancy of this design also makes it more resilient, being able to levitate seamlessly even when one coil fails and disconnects.

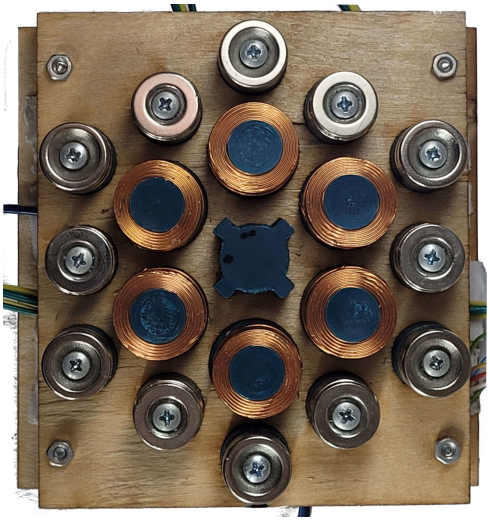


Figure 4.12: Modular set used to build a 6-coil platform with coreless coils.

4.3.3 Lifting forces

In the same way as in the previous section, we modeled the lifting force of 4 coils running 1 A of current each. This time we moved all the coils closer or farther from the center, measuring how the lifting force changed with distance. The results of this simulation are shown in Figure 4.13.

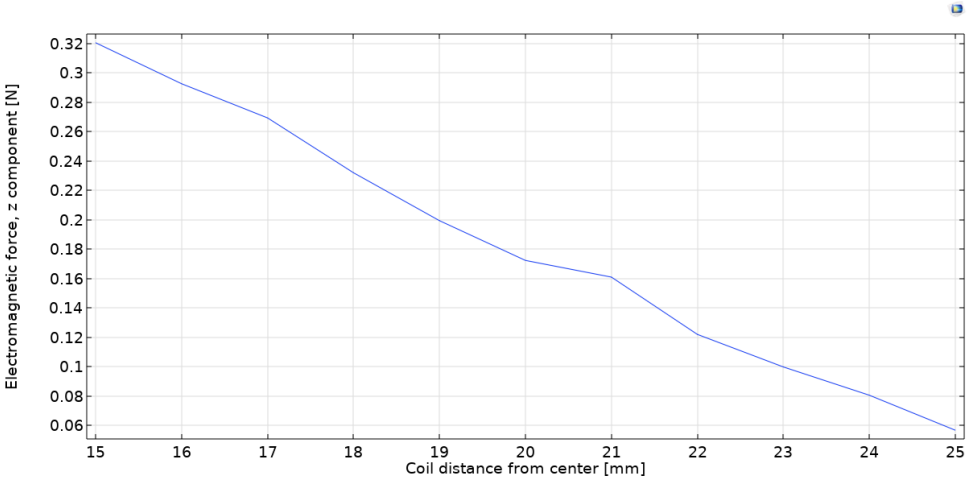


Figure 4.13: Lifting force of 4 coils running 1 A of current each based on their distance from the center of the platform.

The lifting forces drop rapidly as the coils move away from the center. In order to maximize the lifting force, placing the coils as close as possible to the center is desirable. For maximum lifting force, using fewer coils and placing them more close together is beneficial; however, this reduces the total lateral (XY) stabilizing force that the coils are able to project. Using more coils, but slightly farther away, can be a good compromise. Another option would be

to place the coil directly in the center around the hall sensors, but this might deteriorate the precision of position measurements.

4.4 Rotation

To enable rotation of the levitating magnet, we added two small neodymium magnets to its top, as shown in Figure 4.14. These additions do not significantly change the magnetic field of the main magnet, but will allow us to apply a torque using this small inhomogeneity in the normally rotational-symmetric magnet.

We need to change the magnetic field produced by the coils in order to exert torque on the magnet, but without moving it around in the XY plane. This is difficult to do with only four coils, as we have only two coils per axis. To solve this, we added two extra coils, making a total of six. The whole coil and magnet setup is visible in Figure 4.1.

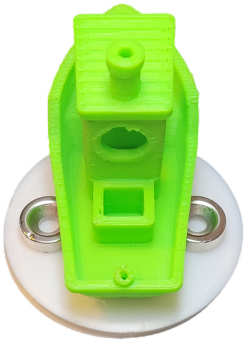


Figure 4.14: Two added magnets to the levitation magnet in order to enable rotation.

4.4.1 Stabilizing rotation

With the 6-coil setup, we found a way to control the magnetic field in a way that applies torque to the levitating magnet, but no horizontal force. In order to create a stronger field in a given axis, we would actuate the two coils composing this axis in the positive orientation and all of the other four coils in the negative orientation. Effectively, we added the pattern to the coil actuation values

$$\text{coil\_values} \mathrel{+}= [1, -1,\ 1,\ 1, -1,\ 1] \cdot \text{strength}\,.$$

This creates an inhomogeneous magnetic field, as is visible in a snapshot from the FEM simulation of the fields in Figure 4.15 while keeping the net horizontal forces balanced, so the magnet stays centered. This makes the magnet align with the stronger axis of the field. However, this causes the magnet to stabilize in rotation and return to the specified angle after perturbation, with a lot of oscillations.

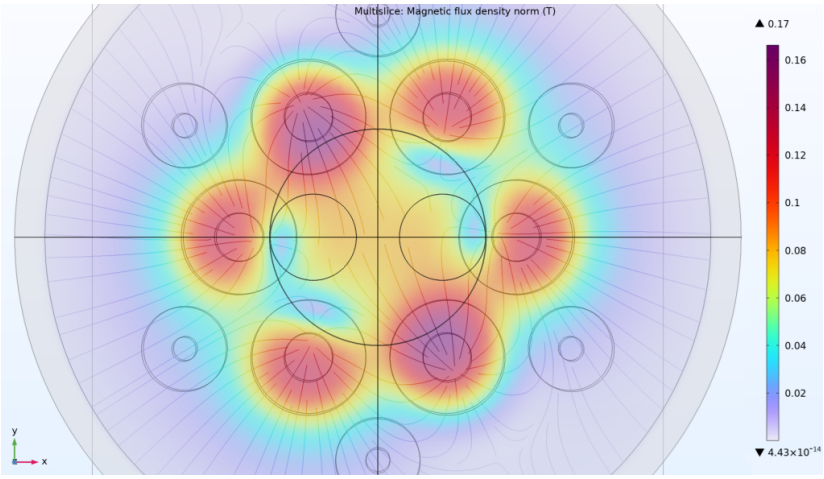


Figure 4.15: Magnetic intensity norm above the coils, with the pattern above applied in the clockwise orientation.

4.4.2 Rotating pattern

To rotate the levitating magnet, we slowly shift the current pattern around the six coils. This is done by smoothly changing the coils to which the pattern is applied over time. We use cosine interpolation with the function $\frac{\cos(\theta)+1}{2}$ to gradually transition the current values between coils as the pattern rotates. Both slow and fast rotation speeds were tested. Because the system has very little damping in rotation, the magnet starts to rotate even with little torque applied by the slight axial orientation of the magnetic field.

4.4.3 Controlling rotation

In a perfectly rotationally symmetric magnetic field, the magnet should rotate freely when it is spinned up. This was not the case, which was most evident at low speeds. The slowly rotating magnet did often stop and would start turning in the other direction. This is probably caused due to tolerances in manufacturing of magnets and the built of the platform, and also by the slight tilt of the rotating magnet.

Using this approach, we can get the magnet to rotate in either direction, with some time needed for the magnet to spin up. Once the magnet reached a speed of about 60 RPM, we were able to sustain this rotation. Speed control was also possible to some extent.

In order to reach slow rotation speeds and more controlled rotation, we would need to measure the angle of the magnet and rotate the magnet using the rotation pattern in accordance with the current angle. Some ways of measuring the angle of the levitating magnet include using magnetic encoders or cameras. However, both of these methods would require the addition of external hardware both to the levitating magnet and to the platform.

Chapter 5

Conclusion

5.1 Applications

One visually interesting application of this levitation system is using the magnet to draw a pattern in a thin layer of sand or other material. We can directly use the flat magnet, as described in this thesis, with a small notch below to shape the sand. Since a larger stabilizing force is needed for this application, to push the sand away, a 6-coil setup would help. It would allow for up to 0.32 N of radial force, at 1 A of current per coil, which should be enough for the magnet to remain stable while moving the sand. Elevation adjustment, which was developed in this thesis, can be used to lift the magnet above the sand and draw non-continuous patterns.



Figure 5.1: A ball magnet levitated above the platform.

We can also use the platform to levitate a neodymium ball magnet, rather than the flat cylinder as this would be more suitable for drawing into the sand. The levitated ball is visible in Figure 5.1.

5.2 Achievements

In this thesis, we described and developed a modular experimental platform for magnetic levitation capable of controlling the position and rotating the levitating permanent magnet. The system combines neodymium magnets and electromagnetic coils, with precise position sensing provided by Hall effect sensors. A real-time PD controller implemented on an STM32 microcontroller ensures stable levitation in all three axes. To address sensor interference from the coils, compensation methods were designed, eliminating the need for external sensing devices used in many related works, making the platform compact and inexpensive. The theoretical results, backed up by numerical simulations, give insight into the inner workings of the system, allowing us to analyze the forces exerted on the object and design an appropriate and reliable controller. They are also useful for developing different arrangements of the platform and finding variants tailored to as specific application. Due to its open and configurable modular design, this platform accommodates different types of levitating magnet, making it possible to develop applications that are not easily achieved with the currently available magnetic platforms.

Appendix A

Images

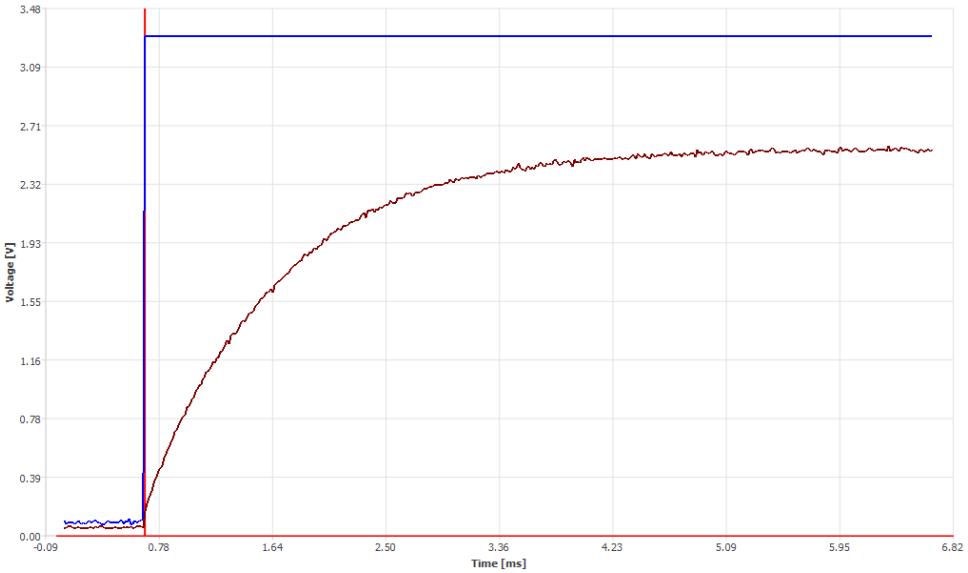


Figure A.1: Current response of coils to step voltage. Voltage applied to coil in blue, coil current in brown (with a ration of 1.1 V/A).

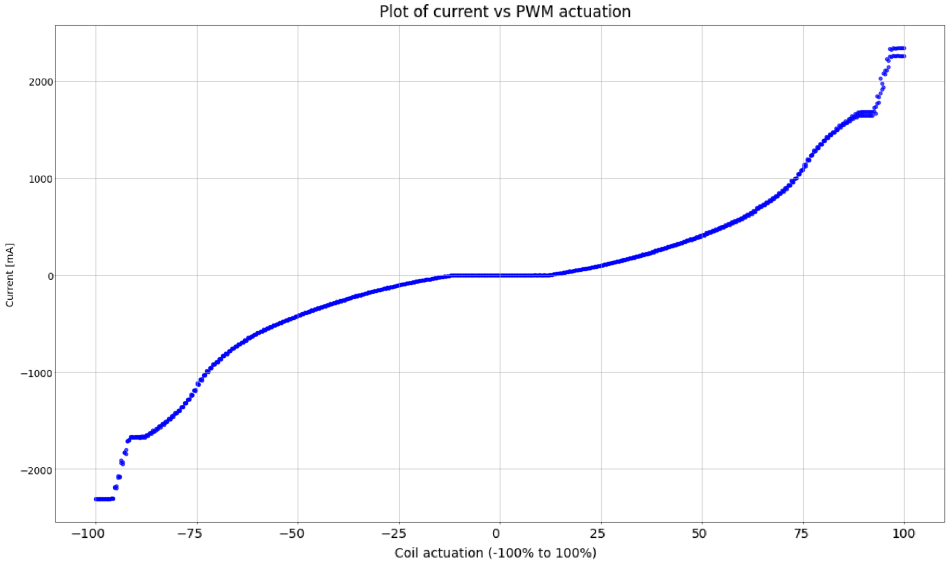


Figure A.2: Relationship between duty cycle and current, in *Phase* drive mode.

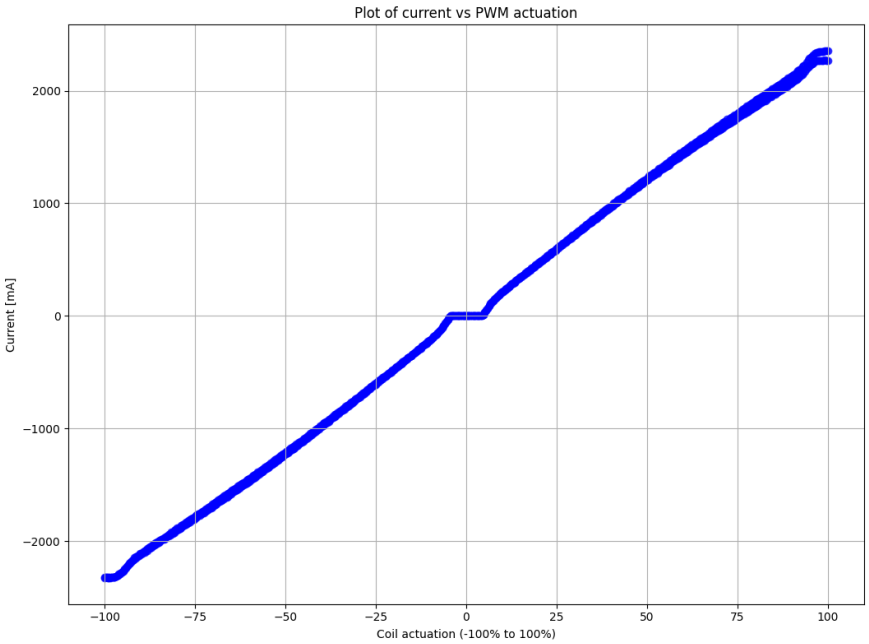


Figure A.3: Relationship between duty cycle and current, in *Phase/Enable* drive mode with PWM frequency of 64 kHz.

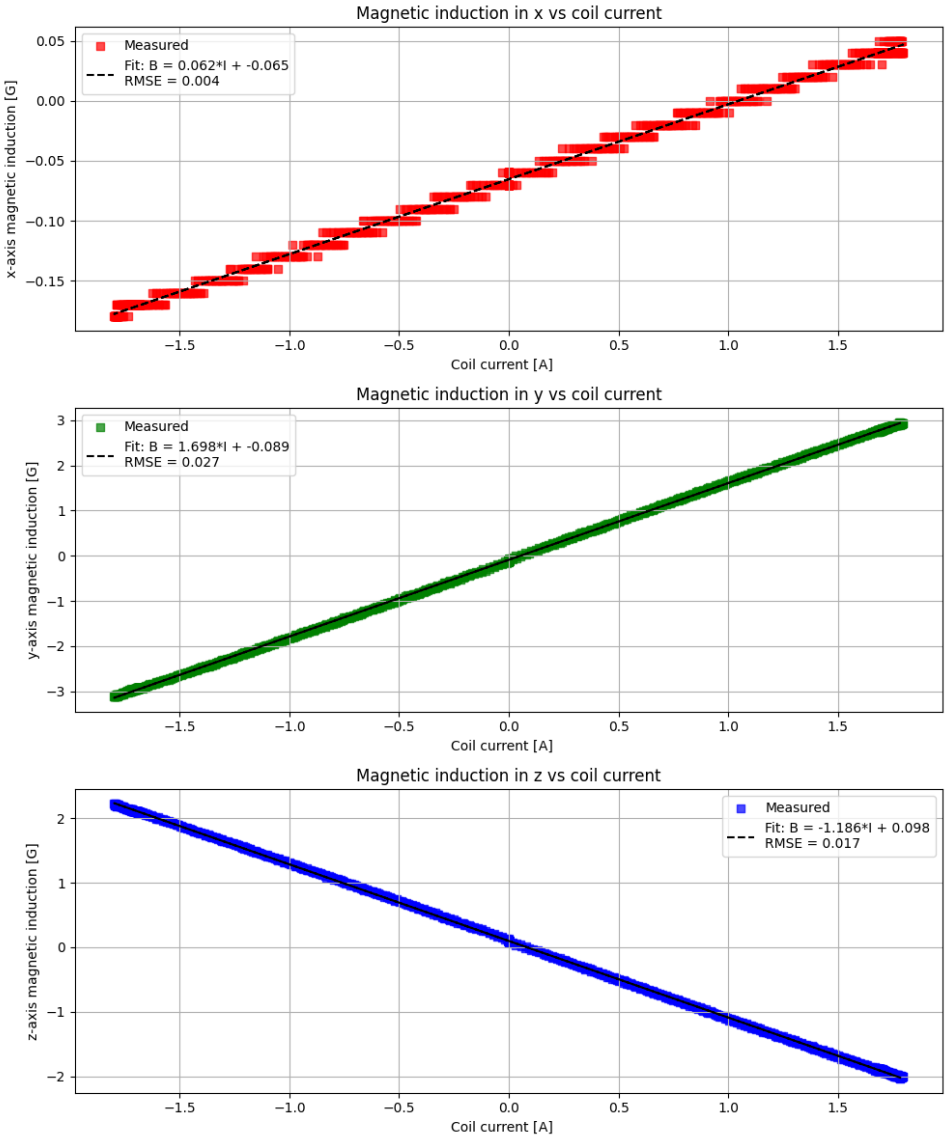


Figure A.4: Magnetic induction above the platform for coils with no core, fitted with a linear function, for all three axes.

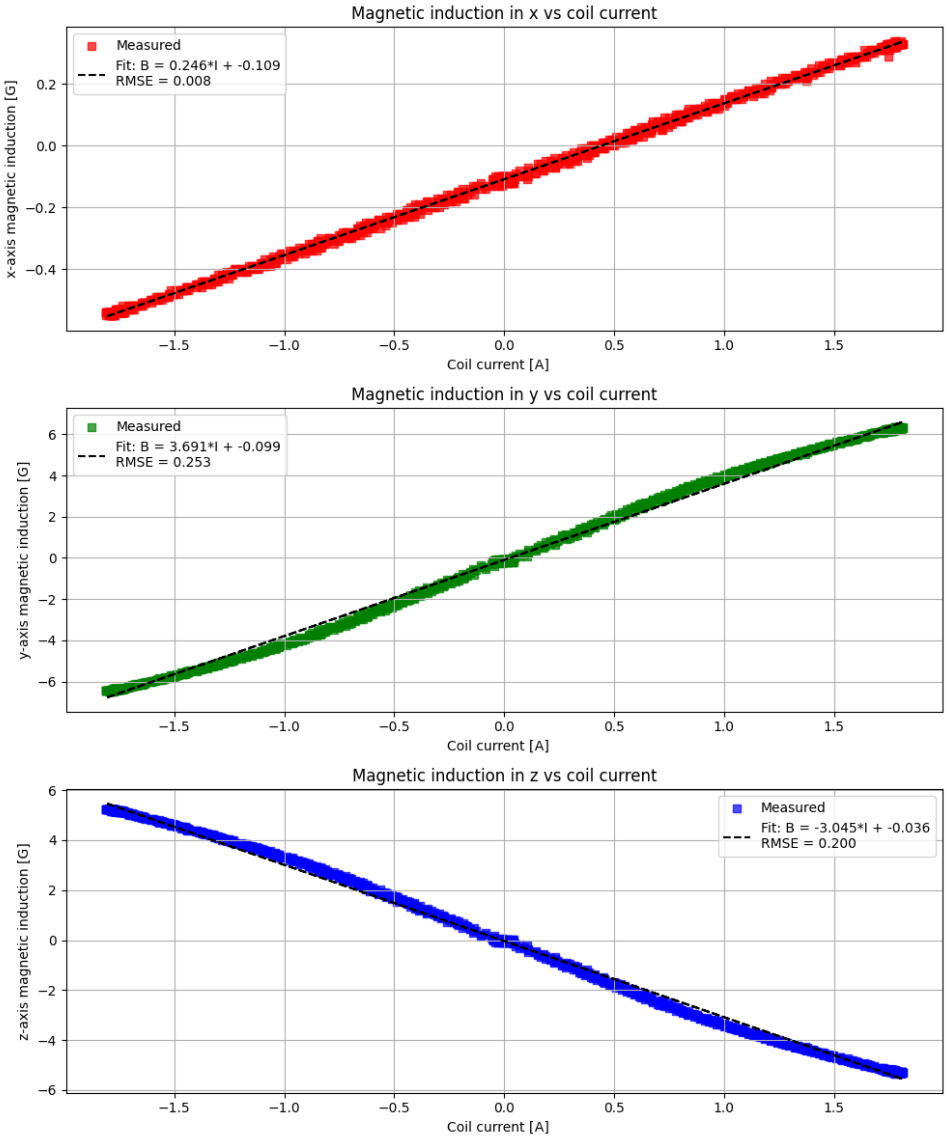


Figure A.5: Magnetic induction above the platform for coils with no ferromagnetic cores, fitted with a linear function, for all three axes.

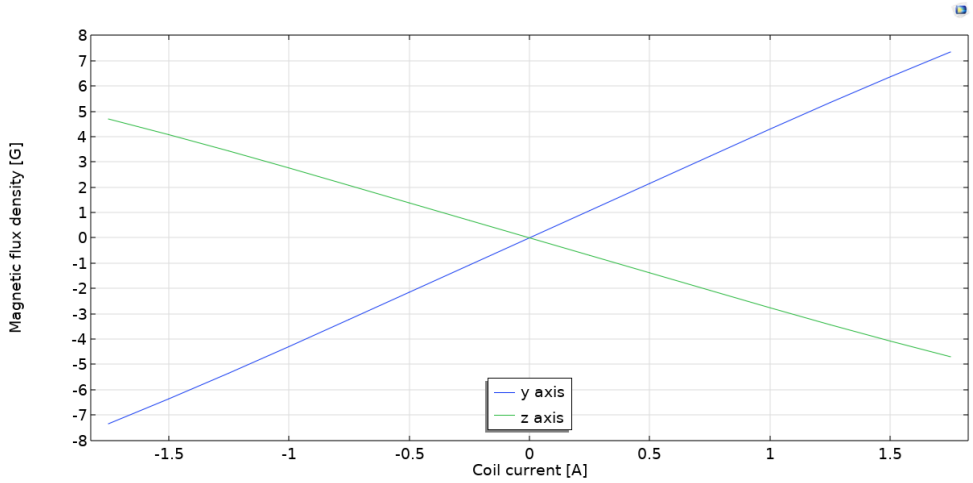


Figure A.6: Simulation of magnetic induction above the platform for coils with no core.

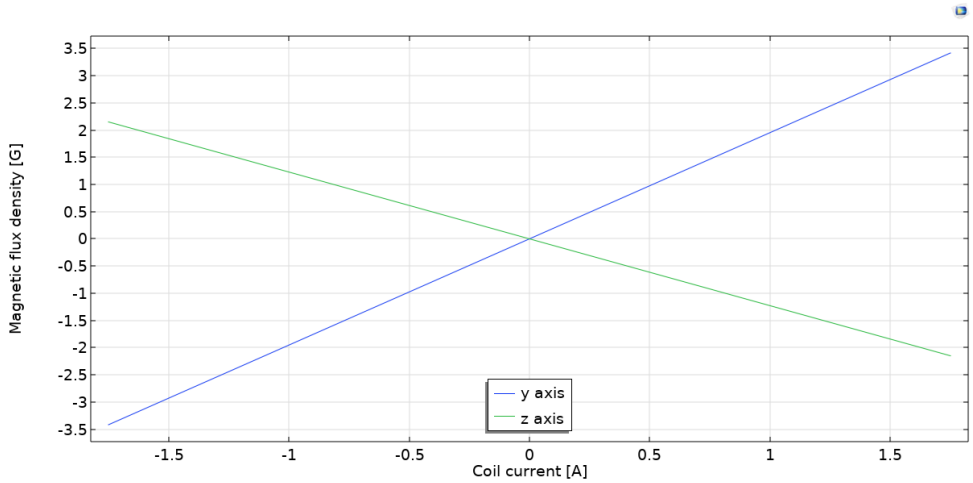


Figure A.7: Simulation of magnetic induction above the platform for coils with no ferromagnetic cores.

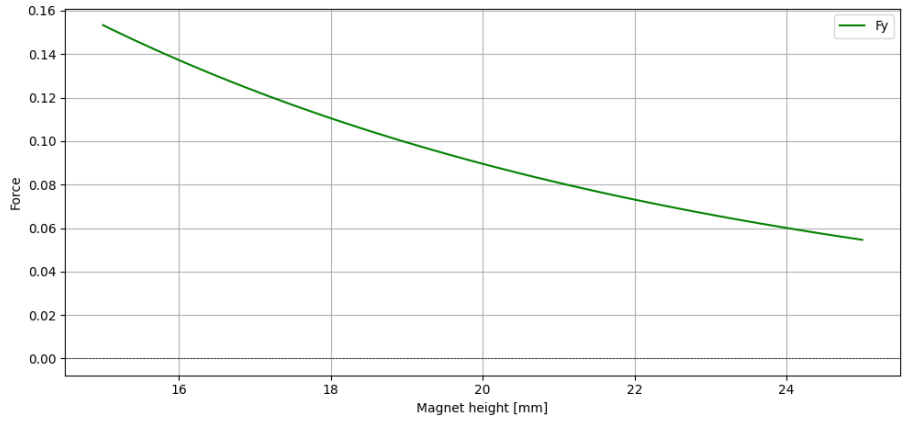


Figure A.8: Prediction of the coil force as given by Equation 3.16.

Appendix B

Bibliography

[1] Honeywell International Inc. *SS39ET/SS49E/SS59ET Series Linear Hall-effect Sensor ICs*, 2015.

[2] Shenzhen Hongxin Hardware Co., Ltd. Electric Coil Size 12x19mm/0.47x0.75inches Durable, 2024.

[3] UNIMAGNET s.r.o., 2025. `https://www.unimagnet.cz/`.

[4] Onsemi. *LM324 Single Supply Quad Operational Amplifiers*, 2019. `https://www.onsemi.com/pdf/datasheet/lm324-d.pdf`.

[5] Kenneth L. Kaiser. *Electromagnetic compatibility handbook*. CRC Press, 2004.

[6] Hamid Yaghoubi. The most important maglev applications. *Journal of Engineering*, 2013. `https://www.researchgate.net/publication/258395126_The_Most_Important_Maglev_Applications`.

[7] Roberto Bassani. Earnshaw (1805–1888) and passive magnetic levitation. *Meccanica*, 41:375–389, 2006. `https://link.springer.com/article/10.1007/s11012-005-4503-x`.

[8] Peter Berkelman and Michael Dzadovsky. Magnetic levitation over large translation and rotation ranges in all directions. *IEEE/ASME Transactions on Mechatronics*, 18(1):44–52, 2013.

[9] Anand Bala Subramaniam, Dian Yang, Hai-Dong Yu, Alex Nemiroski, Simon Tricard, Audrey K. Ellerbee, Siowling Soh, and George M. Whitesides. Noncontact orientation of objects in three-dimensional space using magnetic levitation. *Proceedings of the National Academy of Sciences*, 111(36):12980–12985, 2014.

[10] Brian Nils Hansen. Method and apparatus for magnetic levitation, U.S. Patent US6595041B2, 2001.

[11] K&J Magnetics. Electromagnetic Levitation. `https://www.kjmagnetics.com/blog/electromagnetic-levitation`.

[12] Jiří Hospodka. *Elektronické obvody*. ČVUT FEL, 2024.

[13] Texas Instruments. *DRV8874-Q1 H-Bridge Motor Driver With Integrated Current Sense and Regulation*, Jan. 2021. https://www.ti.com/lit/ds/symlink/drv8874-q1.pdf.

[14] Pololu Corporation. DRV8874 Single Brushed DC Motor Driver Carrier, 2021. https://www.pololu.com/product/4035.

[15] STMicroelectronics. *STM32F411xC STM32F411xE - Arm® Cortex® -M4 32b MCU+FPU, 125 DMIPS, 512KB Flash, 128KB RAM, USB OTG FS, 11 TIMs, 1 ADC, 13 comm. interfaces*, 2024. https://www.st.com/resource/en/datasheet/stm32f411re.pdf.

[16] Tai L. Chow. *Introduction to electromagnetic theory: A modern perspective*. Jones and Bartlett Publishers, 2006.

[17] Jiří Zemánek. *Distributed manipulation by controlling force fields through arrays of actuators*. ČVUT FEL, 2018.

[18] COMSOL, Inc. AC/DC Module - User's guide, 2021. https://doc.comsol.com/6.0/doc/com.comsol.help.acdc/ACDCModuleUsersGuide.pdf.

[19] Stm32duino. Arduino core support for STM32 based boards, 2025. https://github.com/stm32duino/Arduino_Core_STM32.

[20] Microchip Technology Inc. *MCP3004;MCP3008 2.7V 10-Bit A/D Converters with SPI Interface*, 2022. https://ww1.microchip.com/downloads/aemDocuments/documents/MSLD/ProductDocuments/DataSheets/MCP3004-MCP3008-Data-Sheet-DS20001295.pdf.

[21] Sysprogs. A detailed tutorial on STM32 ADC , 2015. https://visualgdb.com/tutorials/arm/stm32/adc/.

[22] Walter Frei, COMSOL, Inc. Modeling electromagnetic coils. https://www.comsol.com/support/learning-center/article/modeling-electromagnetic-coils-8251/112.

[23] STMicroelectronics. *STM32 Cortex® -M4 MCUs and MPUs programming manual*, 2020.